submitted to *Geophys. J. Int.*

Parallel 3D marine controlled-source electromagnetic modeling using high-order tetrahedral Nédélec elements

Octavio Castillo-Reyes[1], Josep de la Puente[1], Luis Emilio García-Castillo[2] and José M

[1] *Barcelona Supercomputing Center (BSC), Barcelona, Spain. Email: octavio.castillo@bsc.es*

[2] *Department of Signal Theory and Communications, University Carlos III of Madrid, Madrid, Spain.*

SUMMARY

We present a parallel and high-order Nédélec finite element solution for the marine controlled-source electromagnetic (CSEM) forward problem in 3D media with isotropic conductivity. Our parallel Python code is implemented on unstructured tetrahedral meshes, which supports multiple-scale structures and bathymetry for general marine 3D CSEM modeling applications. Based on a primary/secondary field approach, we solve the diffusive form of Maxwell's equations in the low-frequency domain. We investigate the accuracy and performance advantages of our new high-order algorithm against a low-order implementation proposed in our previous work. The numerical precision of our high-order method has been successfully verified by comparisons against previously published results that are relevant in terms of scale and geological properties. A convergence study confirms that high-order polynomials offer a better trade-off between accuracy and computation time. However, the optimum choice of the polynomial order depends on both the input model and the required accuracy as revealed by our tests. Also, we extend our adaptive-meshing strategy to high-order tetrahedral elements. By using adapted-meshes to both physical parameters and high-order schemes, we are able to achieve a significant reduction

in computational cost without sacrificing accuracy in the modeling. Furthermore, we demonstrate the excellent performance and quasi-linear scaling of our implementation in a state-of-the-art HPC architecture.

Key words: Marine CSEM, numerical solutions, high-order Nédélec elements, high-performance computing.

1 INTRODUCTION

The 3D Controlled-source electromagnetic method (3D CSEM) has been widely used in geophysics for a diverse suite of applications across mineral and resource mining (Sheard *et al.* 2005; Yang *et al.* 2012), crustal conductivity studies (Hördt *et al.* 1992; Hördt *et al.* 2000), CO_2 storage characterization (Girard *et al.* 2011), geothermal reservoir imaging (Coppo *et al.* 2016), and off-shore hydrocarbon exploration (Newman *et al.* 1997; Eidesmo *et al.* 2002; Avdeev, *et al.* 2005; Constable 2006; Srnka *et al.* 2006; Orange *et al.* 2009; Constable 2010; Börner 2010)

Rigorous interpretation of electromagnetic (EM) data in complex geological environments requires accurate and efficient modeling tools. By using these tools, Maxwell's diffusive equations in the low-frequency range are solved to obtain a prediction of the EM response. The response depends on the distribution of geological properties and the type of excitation source. According to the conductivity, the medium may be classified as isotropic or anisotropic. Sources, on the other hand, may be categorized as source type (e.g., electric or magnetic dipole) and source signal (e.g., time-harmonic, direct current, or transient).

Marine CSEM modeling algorithms are based on four major approaches: Integral Equations (IE) (Xiong *et al.* 1997; Zhdanov *et al.* 2006; Bakr *et al.* 2009), Finite Differences (FD) (Newman *et al.* 1997; Davydycheva *et al.* 2003; Newman *et al.* 2010), Finite Volumes (FV) (Hermeline 2009; Jahandari and Farquharson 2014), and Finite Elements (FE) (Schwarzbach 2009; Key *et al.* 2011; Koldan *et al.* 2014).

At the computational level, the conventional IE method results in a dense system of equations and works efficiently for simple conductivity models. However, its computational cost increases with the model complexity (e.g., models containing multiple layers) (Streich *et al.* 2009; Ansari *et al.* 2014). On the other hand, FD, FV, and FE schemes, lead to sparse systems of equations. The FD methods' popularity is mainly due to their simple domain discretisation by using regular grids. As a drawback, FD methods can only approximate complex geological structures using a stair-case approach. Thus, grid sizes can quickly increase

when model structures do not fit rectangular meshes, as those models exhibiting realistic bathymetry or containing physical features of different spatial scales. It is worth to mention that octree grids (semi-unstructured meshes) offer more flexibility by dividing the hexahedral elements close to the refinement region into smaller cells. However, this approach is restricted at some point due to regular meshes limitations (Haber and Heldmann 2007; Jahandari *et al.* 2017). FV methods discretize the integral form of the governing equations, which offers a more straightforward mathematical formulation. Moreover, the generalized FV schemes (e.g., cell-centered and staggered) can be applied to unstructured meshes.

Recently, FE methods have gained popularity in the context of 3D CSEM modeling. Compared to FD methods, FE methods allow precise representations regarding model geometry without such a severe increase in problem sizes. For accurate node-based FE solutions, the divergence-free condition for the EM fields needs to be imposed to mitigate possible spurious solutions in the computational domain (Salazar-Palma *et al.* 1998; Jin 2002). A conventional approach to deal with this obstacle is to formulate the 3D CSEM problem in terms of its electric potentials. However, numerical convergence can drop due to numerical differentiation is required to compute EM responses (Badea *et al.* 2001; Um *et al.* 2010; Puzyrev *et al.* 2013).

We avoid the spurious solutions by implementing the Nédélec FE method which provides stable numerical solutions by means of proper modeling (discretisation) of the $\mathbf{H}(\mathrm{curl})$ space to which the EM field belongs to (Nédélec 1980; Salazar-Palma *et al.* 1998; García-Castillo *et al.* 2000; Jin 2002; García-Castillo *et al.* 2002). The Nédélec FE basis functions are capable of ensuring tangential continuity of the fields on the element's interfaces while the normal components are allowed to be discontinuous. Furthermore, since Nédélec schemes belong to the class of FE, they are well suited for honoring complex geometrical structures such as realistic geology or bathymetry. Given its advantages for electromagnetic modeling, Nédélec FE have recently been employed for 3D CSEM modeling, either using low-order basis functions (Cai *et al.* 2014; Chung *et al.* 2014; Cai *et al.* 2015) or high-order polynomials (Schwarzbach *et al.* 2011; Grayver and Kolev 2015; Rochlitz *et al.* 2019). Also, there are important computational applications to geophysical EM modeling such as *DIPOLE1D* (Key 2009), *AarhusInv* (Auken *et al.* 2014), *empymod* (Werthmüller 2017), and *custEM* (Rochlitz *et al.* 2019). However, with the sole exception of the algorithm developed by Rochlitz *et al.* (2019), none are capable to deal with arbitrary marine CSEM modeling applications and they are either sequential or black-box packages.

In this paper, we present a Nédélec FE algorithm with second and third order accuracy for the efficient solution of marine 3D CSEM problems. This systematic approach is an extension

of our previously published scheme in Castillo-Reyes *et al.* (2018), where a first order method has been implemented and studied. Therefore, we investigate the advantages of our new high-order algorithm regarding convergence rate, accuracy, and computational cost. In addition, we extend our tetrahedral adaptive-meshing technique to high-order Nédélec FE. As a result, the mesh generation process is guided by both the physical parameters and polynomial order to satisfy the chosen quality criteria. Building on and extending third-party libraries, we have implemented a new version of *PETGEM* (Parallel Edge-based Tool for Geophysical Electromagnetic Modelling), which features unstructured adapted meshes, high-order polynomial approximations, simple and clear Python syntax, and support for high-performance computing (HPC) architectures. Furthermore, our code is open-source under the GPLv3 license. Clearly, this facilitates its efficient deployment on diverse computing platforms and the solution of test cases that are realistic regarding both spatial scales and geological properties.

Section 2 states the formulation and implementation of our numerical method. Firstly, we present some theoretical background on the governing equations of marine 3D CSEM. Secondly, we introduce the 2^{nd} and 3^{rd} order Nédélec FE approximation to the electric field diffusion equation. Thirdly, we present the implementation details of the parallel algorithm with emphasis on the new version of our adaptive-meshing technique. In Section 3, we describe and analyze *PETGEM* solutions versus numerical tests and emphasize the method's features and virtues. Firstly, a convergence study provides numerical evidence that the use of higher-order Nédélec FE are beneficial for the solution of the problem under consideration. Secondly, through comparison with other state of the art algorithms, we describe the application of the code to realistic marine 3D CSEM models on HPC platforms. Finally, a strong-scaling study shows the parallel efficiency of our implementation. Section 4 provides conclusions and summary remarks.

2 THEORY

2.1 Governing equations

The marine 3D CSEM problem is governed by the Maxwell's equations in their diffusive form (Zhdanov 2009). We consider a 3D isotropic conductivity model whose coordinate system is right-handed with the z-axis pointing downwards. A horizontal electric dipole (HED), also referred to as source, is located above the seafloor. By assuming a time-harmonic source dependence $e^{-i\omega t}$, the governing equations for the electric field ($\mathbf{E}$) and magnetic field ($\mathbf{H}$) in

quasi-stationary form are

$$\nabla \times \mathbf{E} = i\omega\mu_0\mathbf{H}, \tag{1}$$

$$\nabla \times \mathbf{H} = \mathbf{J}_\mathrm{s} + \sigma\mathbf{E}, \tag{2}$$

where ω is the angular frequency, μ_0 is the free-space magnetic permeability, $\mathbf{J}_\mathrm{s}$ is the distribution of source current, $\sigma\mathbf{E}$ is the induced current in the conductive Earth, and σ is the isotropic conductivity.

After substituting eq. (1) into eq. (2), we obtain

$$\nabla \times \nabla \times \mathbf{E} + i\omega\mu_0\sigma\mathbf{E} = i\omega\mu_0\mathbf{J}_\mathrm{s}, \tag{3}$$

which is known as the curl-curl formulation of the problem. One technique for solving eq. (3) is to split the electric field into primary ($\mathbf{E}_\mathrm{p}$) and secondary ($\mathbf{E}_\mathrm{s}$) components, corresponding to the electric field arising from some reference conductivity model σ_p, and the field arising from the conductivity difference $\sigma_\mathrm{s} = \sigma - \sigma_\mathrm{p}$ with respect to the model of interest (Newman and Alumbaugh, 1995; Alumbaugh *et al.* 1996). Based on this approach, the total electric field is found by summing the respective components

$$\mathbf{E} = \mathbf{E}_\mathrm{p} + \mathbf{E}_\mathrm{s}. \tag{4}$$

The primary electric field for the reference model σ_p, also referred to as background model, can be calculated analytically in simple cases, which means that $\mathbf{E}_\mathrm{p}$ admits a well-behaved solution. In our case, the reference model is assumed to be homogeneous. The main advantage of this technique lies in the fact that the source-singularities are removed from the numerical calculations of the secondary field. In addition, the FE mesh only needs to accurately capture the secondary field which is much smoother than the primary component. Consequently, a mesh with fewer elements can often be used, thus reducing the computational cost.

After applying the electric field decomposition, eq. (3) becomes

$$\nabla \times \nabla \times \mathbf{E}_\mathrm{s} + i\omega\mu_0\sigma\mathbf{E}_\mathrm{s} = -i\omega\mu_0\sigma_\mathrm{s}\mathbf{E}_\mathrm{p}, \tag{5}$$

which is the equation to be solved. It is easy to see that the right-hand side of eq. (5) can be described as a source term resulting from the inhomogeneities between σ_s and $\mathbf{E}_\mathrm{p}$. To solve eq. (5) for the unknown electric field $\mathbf{E}_\mathrm{s}$, homogeneous Dirichlet boundary conditions are applied on the outer boundary of the model. The range of applicability of this condition can be determined based on the skin depth (δ) of the electric field $\mathbf{E}$ (Plessix *et al.* 2007).

2.2 High-order Nédélec finite element method

For the computation of the electric field $\mathbf{E}_\mathrm{s}$ we have used tetrahedral FE conforming in $\mathbf{H}(\mathrm{curl})$, which is the space of square-integrable functions whose curl is also square-integrable. Therefore, $\mathbf{H}(\mathrm{curl})$ is the appropriate function space to discretise $\mathbf{E}_\mathrm{s}$ in eq. (5). Specifically, the FE used here belongs to the so-called mixed-order scheme proposed by Nédélec (1980). Its elements provide a mixed-order approximation of the vector field while the approximation of the curl remains complete and of one order less (as in their complete order counterpart). In the following, we introduce our methodology to obtain mixed-order curl-conforming basis functions.

2.2.1 Basis function space

Within a tetrahedral element e, $\mathbf{E}_\mathrm{s}$ can be obtained as follows

$$\mathbf{E}_\mathrm{s}^e(\tilde{x}) = \sum_{i=1}^{n_p} \mathbf{N}_i(\tilde{x}) E_i^e, \tag{6}$$

where $\mathbf{N}_i$ are the curl-conforming basis functions, n_p is the total number of basis functions for a p-th order Nédélec FE scheme, and E_i^e is their respective degrees of freedom (dof).

The space of basis functions $\mathbf{N}_i$ of order p for the tetrahedron, $\boldsymbol{\mathcal{R}}_p$, corresponds to the Nédélec space for the 3D simplex. The Nédélec space for simplices of order p is uniquely defined in Nédélec (1980). For the 2$^{\mathrm{nd}}$ order case, $\boldsymbol{\mathcal{R}}_2$ can be expressed as linear combination of monomials

$$\boldsymbol{\mathcal{R}}_2 \equiv \left\{ \begin{array}{l} a_1 + a_2\xi + a_3\eta + a_4\zeta + D\eta^2 - F\xi\eta - G\xi\zeta + H\zeta^2 + J\eta\zeta \\ b_1 + b_2\xi + b_3\eta + b_4\zeta - D\xi\eta - E\eta\zeta + F\xi^2 + I\zeta^2 - J\xi\zeta + K\xi\zeta \\ c_1 + c_2\xi + c_3\eta + c_4\zeta + E\eta^2 + G\xi^2 - H\xi\zeta - I\eta\zeta - K\xi\eta \end{array} \right\}, \tag{7}$$

where the 20 coefficients $a_1, a_2, \ldots, b_1, b_2, \ldots, c_1, c_2, \ldots, D, E, \ldots, K$ of the linear combination are real numbers. Thus, the dimension of $\boldsymbol{\mathcal{R}}_2$ is 20.

On the other side, for the 3$^{\mathrm{rd}}$ order scheme, $\boldsymbol{\mathcal{R}}_3$ can be written analogously as

$$\boldsymbol{\mathcal{R}}_3 \equiv \left\{ \begin{array}{l} a_1 + a_2\xi + a_3\eta + a_4\zeta + a_5\xi^2 + a_6\eta^2 + a_7\zeta^2 + a_8\xi\eta + a_9\xi\zeta + a_{10}\eta\zeta + D\xi^2\eta \\ b_1 + b_2\xi + b_3\eta + b_4\zeta + b_5\xi^2 + b_6\eta^2 + b_7\zeta^2 + b_8\xi\eta + b_9\xi\zeta + b_{10}\eta\zeta - D\xi^3 \\ c_1 + c_2\xi + c_3\eta + c_4\zeta + c_5\xi^2 + c_6\eta^2 + c_7\zeta^2 + c_8\xi\eta + c_9\xi\zeta + c_{10}\eta\zeta + F\zeta^2\xi \end{array} \right. + \left. \begin{array}{l} -E\eta^3 - F\zeta^3 + G\xi^2\zeta + J\eta^2\xi + K\zeta^2\xi + M\xi\eta\zeta - O\eta^2\zeta + P\eta^2\zeta - Q\zeta^2\eta + R\zeta^2\eta \\ +E\eta^2\xi - H\zeta^3 + I\eta^2\zeta - J\xi^2\eta + L\zeta^2\eta - M\xi^2\zeta + N\xi^2\zeta + O\xi\eta\zeta - R\zeta^2\xi \\ -G\xi^3 + H\zeta^2\eta - I\eta^3 - K\xi^2\zeta - L\eta^2\zeta - N\xi^2\eta - P\eta^2\xi + Q\xi\eta\zeta \end{array} \right\}, \tag{8}$$

where the 45 coefficients $a_1, a_2, \ldots, b_1, b_2, \ldots, c_1, c_2, \ldots, D, E, \ldots, R$ are also real numbers. Thus, the dimension of $\boldsymbol{\mathcal{R}}_3$ is 45.

The space $\boldsymbol{\mathcal{R}}_p$ for p-th order basis may also be written as

$$\boldsymbol{\mathcal{R}}_p = \mathbf{P}_{p-1} \oplus \boldsymbol{\mathcal{S}}_p, \tag{9}$$

where the elements of space $\boldsymbol{\mathcal{S}}_p$ are homogeneous polynomials $\boldsymbol{u}$ of order p, satisfying the so-called Nédélec constraints. The symbol $\oplus$ denotes direct sum. For the sake of clarity, we point out that direct sum decomposition in eq. (9) is easily observed in explicit expressions of eq. (7) and eq. (8).

For the sake of convenience, we compute the basis functions $\mathbf{N}_i$ over a reference element r. The basis functions $\mathbf{N}_i^r$ are not given but obtained as a base of *a priori* defined basis functions space. This implies the use of space $\boldsymbol{\mathcal{R}}_p$ by determining the sets of values of the coefficients for $\boldsymbol{\mathcal{R}}_2$ and $\boldsymbol{\mathcal{R}}_3$, in such a way that the resulting basis functions $\mathbf{N}_i^r$ are linearly independent. This procedure has the advantage of assuring the properties of the space of functions spanned by FE basis functions $\mathbf{N}_i$, which determine the stability and convergence properties of the numerical scheme. Consequently, the basis functions $\mathbf{N}_i$ are obtained as dual basis with respect to a set of unisolvent dof acting on the defined space (e.g., classic FE definition by Ciarlet (1994)). Therefore, we define unisolvent dof functionals $g_j(\boldsymbol{u})$ where $\boldsymbol{u} \in \boldsymbol{\mathcal{R}}_p$. More explicitly,

$$g_j(\mathbf{N}_i) = \delta_{ji}, \quad j, i = 1 \dots n, \tag{10}$$

where δ_{ji} is the Kronecker delta, n is 20 for $p = 2$ and 45 for $p = 3$. Note that, once discrete versions of functional dof g_j are defined, eq. (10) results in an algebraic system of equations of dimension 20×20 for $p = 2$, and 45×45 for $p = 3$. In this linear system, the right-hand side is the identity matrix, and the unknown vector contains the coefficients of eq. (7) or eq. (8) for each order p.

Then, the basis function $\mathbf{N}_i$ on a given real element of the mesh is obtained by using

$$\mathbf{N}_i = [\mathbf{J}]^{-1} \mathbf{N}_i^r, \tag{11}$$

where $[\mathbf{J}]^{-1}$ is the Jacobian matrix of the geometric transformation, $\mathbf{N}_i^r$ is the basis function in the reference element r, and $\mathbf{N}_i$ is the resulting mapped basis function in the physical element. One finds that curl-conformity is automatically assured both for elements having straight edges or elements having curved boundaries through the concept of isoparametric elements (Reddy *et al.* 1984).

The procedure described above has demonstrated to be mathematically consistent. This means, in particular, that basis functions $\mathbf{N}_i$ are well-conditioned and provide numerical stability even for higher-order polynomials (García-Castillo *et al.* 2000).

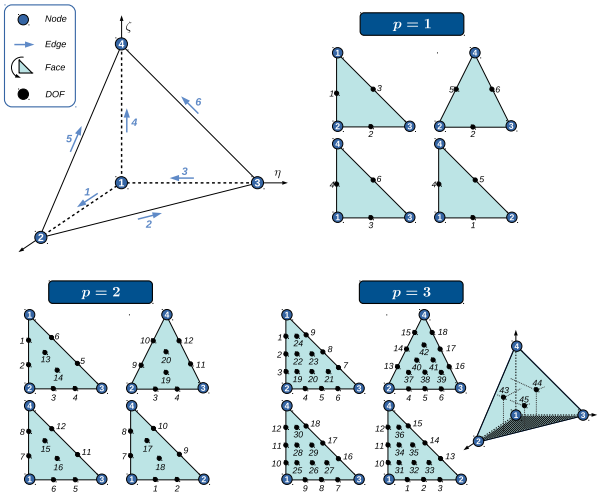

Figure 1. Reference tetrahedral element showing numeration of dof for each order p. For $p = 1$ there are six dof (one per edge). For $p = 2$ there are 20 dof (two per edge and two per face). Finally, in the case of $p = 3$, there are 45 dof (three per edge, six per face and three per element's volume).

2.2.2 Degrees of freedom

In our approach, the functionals g_j are associated to edges, faces and volume of the tetrahedral elements as shown in Figure 1. Hence, the basis functions $\mathbf{N}_i$ are practical for a standard FE assembly procedure. The dof associated to edges are defined as

$$g(\boldsymbol{u}, q) = \int_e (\boldsymbol{u} \cdot \hat{\boldsymbol{\tau}}) q \, dl, \quad \forall q \in \mathbf{P}_{p-1}(e), \tag{12}$$

where e stands for edge, $\hat{\boldsymbol{\tau}}$ is the unit vector tangent to the considered edge, and $\mathbf{P}_{p-1}(e)$ is the space of scalar $(p-1)$-th order polynomials in the corresponding edge local coordinate. There are two dof per edge for $p = 2$, and three dof per edge for $p = 3$. The scalar polynomials q for each dof on edges can be found in Appendix A.

On the other hand, dof associated to triangular faces can be written as

$$g(\boldsymbol{u}, \boldsymbol{q}) = \int_{f_t} (\boldsymbol{u} \times \hat{\boldsymbol{n}}) \cdot \boldsymbol{q} \, ds, \quad \forall \boldsymbol{q} \in \mathbf{P}_{p-2}(f_t), \tag{13}$$

where f_t stands for each triangular face, $\hat{\boldsymbol{n}}$ is the outward unit normal vector to the considered face, and $\mathbf{P}_{p-2}(f_t)$ denotes here the space of two component vector $(p-2)$-th order polynomials in the corresponding two local coordinates of the triangular face. There are two dof per face for $p = 2$, and six dof per face in the case of $p = 3$. The vector polynomials $\boldsymbol{q}$ according to each dof on faces can be found in Appendix A.

Finally, the dof associated to volume (interior) are defined as

$$g(\boldsymbol{u}, \boldsymbol{q}) = \int_\Omega \boldsymbol{u} \cdot \boldsymbol{q} \, ds, \quad \forall \boldsymbol{q} \in (\mathbf{P}_{p-3})^3, \tag{14}$$

where Ω stands for the element volume, and $(\mathbf{P}_{p-3})^3$ is the space of three component vector $(p-3)$-th order polynomials in the corresponding local coordinates of the element. There are three dof for $p = 3$, and none in the case of $p = 2$. The vector polynomials $\boldsymbol{q}$ for this type of dof can be also found in Appendix A.

The practical implementation of dof defined above comes from the discretisation of the polynomial spaces appearing in their definition (scalar q and vector $\boldsymbol{q}$ polynomials). In this case, interpolatory bases, specifically Lagrangian bases, are chosen. Thus, dof, and hence basis functions $\mathbf{N}_i$, can be associated to certain spatial locations within each entity (edge, face, volume) of the tetrahedron (see illustrations in Figure 1).

2.2.3 High-order Nédélec approximation for marine 3D CSEM

Finally, we show explicitly the development to solve $\mathbf{E}_\mathrm{s}$. By substituting eq. (6) into eq. (5), and using Galerkin's approach, the weak form of the original differential equation becomes

$$Q_i = \int_\Omega \mathbf{N}_i \cdot [\boldsymbol{\nabla} \times \boldsymbol{\nabla} \times \mathbf{E}_\mathrm{s} - i\omega\mu_0\sigma\mathbf{E}_\mathrm{s} + i\omega\mu_0\sigma_\mathrm{s}\mathbf{E}_\mathrm{p}]dV. \tag{15}$$

The compact discretized form of eq. (15) is obtained after applying the Green's theorem

$$[K^e_{jk} + i\omega\sigma^e M^e_{jk}] \cdot \{E^e_{sk}\} = -i\omega\mu_0\sigma^e_\mathrm{s} R^e_k, \tag{16}$$

where K^e and M^e are the elemental stiffness and mass matrices. These terms can be calculated analytically or numerically (Jin 2002), whereas R^e_k is the right-hand side requires numerical integration. Furthermore, it is worth to mention that R^e_k can be described as the source term resulting from the inhomogeneities between σ_s and the primary field $\mathbf{E}_\mathrm{p}$.

2.3 Computational implementation

We have implemented our high-order Nédélec FE scheme into *PETGEM* (Parallel Edge-based Tool for Geophysical Electromagnetic Modelling), which is a parallel code for the scalable solution of marine 3D CSEM problems on tetrahedral meshes (Castillo-Reyes *et al.* 2018). *PETGEM* is mostly written in Python 3 and relies on the scientific Python software stack with use of the *mpi4py* (Dalcin *et al.* 2008) and *petsc4py* (Dalcin *et al.* 2011) packages for parallel computation on distributed-memory HPC architectures.

The workflow we follow to carry out marine 3D CSEM modeling can be found in Castillo-Reyes *et al.* (2018); and consists of two overarching stages:

(i) The `Preprocessing`, which provides functionalities to transform physical parameters of a model m into a more suitable format for *PETGEM*.

(ii) The `Kernel`, which is the parallel implementation of the governing equations. Here, the electric field **E** is solved on the computational domain and interpolated at receiver locations afterward.

Although the `Preprocessing` and `Kernel` are executed independently, these two phases must be paired to form all of the components necessary for the solution of a marine 3D CSEM modeling. Further, to compute the electromagnetic responses, `Preprocessing` requires the definition of a physical property model m, describing the conductivity σ, the reference conductivity σ_{p}, the frequency ω, the source S, and receivers locations R. Then, `Kernel` handles the parallel simulation of the physics for the geophysical problem of interest. First, the `kernel` assembles and solves the equation system in parallel. Second, the `kernel` computes the electric fields responses, and these are interpolated to the receiver locations, which are the solution to the problem under consideration. We refer to Castillo-Reyes *et al.* (2018) for a complete discussion of marine 3D CSEM modeling using *PETGEM*. Further, readers interested in more details are referred to the online, up-to-date documentation (http://petgem.bsc.es).

2.3.1 Conductivity model and meshing

Our numerical technique requires the discretisation of continuous functions onto a computational mesh, which defines spatial connectivity, materials locations and domain boundaries. We use *Gmsh* to perform the adapted-mesh generation. Its process is accomplished by using simple Python scripts and calls to routines from *Gmsh*. Furthermore, *PETGEM* supports unstructured tetrahedral meshes which allow us an efficient discretisation of complex domains such as those containing multiple scale structures or bathymetry.

In Castillo-Reyes *et al.* (2018), we introduced an adaptive-meshing strategy for low-order Nédélec FE. The main advantage of this approach was the excellent trade-off between number of dofs and accuracy of the predicted EM responses. As a consequence, we were able to achieve a significant reduction in computational cost (factor of savings of up to four in time and storage). Given its advantages for our modeling purposes, in this paper we extend our preceding adaptive-meshing technique to high-order polynomials.

To point out the similarities and the differences between the present scheme and those described in Castillo-Reyes *et al.* (2018), we summarize the essential aspects of the mesh adaptation technique for low-order Nédélec FE:

(i) Conductivity model definition, which consists of closed volumetric regions (materials) with constant conductivity for each of them. Mesh generation is accomplished semi-

automatically once the volumes are well defined and conductivities are given, as well as the frequency used in the simulation.

(ii) Computation of the skin depth (δ), which is the main quality criteria to determine the global spacing (d_δ) and the dimensions of the computational mesh. This means, in particular, that δ defines an appropriate mesh spacing scale that is consistent with the EM phenomena under consideration.

(iii) Definition of local spacing (d_s) that improves accuracy in regions of interest such as source and receivers positions.

(iv) Inclusion of extra boundary layers, which avoids negative reflections of our imperfect absorbing boundary conditions by enlargening the domain with element sizes increasing logarithmically outwards from the zone of interest.

For more details and proofs, we refer to Castillo-Reyes *et al.* (2018).

The general procedure in this paper is the same as outlined in the four steps above. The main difference is that we deal with the high-order variants defined in Section 2.2. As a result, the incorporation of physical parameters and subsequent responses into the mesh generation process are different. More concretely, we rewrite the rule to compute the global spacing d_δ obtaining

$$d_\delta(f,p) = \frac{\delta_{\min}(f)}{\lambda_\delta(p)}, \tag{17}$$

where f is the frequency (Hz), p is the Nédélec basis order, $\delta_{\min}$ is the minimum skin depth in the model, and λ_δ is the number of points per skin depth that depends both on the basis order p and on the accuracy we aim at reaching. In our previous studies (Castillo-Reyes *et al.* 2018), we have used $\lambda_\delta = 3$ for $p = 1$ to reach errors in amplitude around 1%. However, in this paper we follow a more rigorous methodology to the better estimation of λ_δ for $p = 1, 2, 3$ (see Section 3.1). In any case, λ_δ is chosen prior to building the mesh. For local refinement at sources and receivers locations, we also rewrite the spacing rule d_s as follows

$$d_\mathrm{s} = \min\left(\frac{L_\mathrm{s}}{r_\mathrm{s}(p)}, d_\delta(f,p)\right), \tag{18}$$

where L_s is the source dipole length and r_s is a resolution number between ten and fifteen, which also depends on the order p (see Section 3.1).

Based on this approach, all element sizes are constrained by the global spacing d_δ. When refining the mesh at receivers positions and when embedding the sources, local spacing d_s specifies the size of the mesh according to the distance to such regions. Therefore, the mesh generation process is guided by these parameters to satisfy the chosen quality criteria. Fur-

Basis order	λ_δ	d_δ	r_s	d_s	Elements	dof
$p = 1$	2.5382	153.5033	13	11.6259	1 079 642	1 286 852
$p = 2$	1.0918	356.8621	11	29.2031	144 409	938 506
$p = 3$	0.9433	413.0415	10	39.9459	47 652	901 308

Table 1: Adapted-mesh statistics for a 3D variation on the model proposed by Li *et al.* (2007). For each Nédélec FE basis polynomial degrees $p = 1, 2, 3$, we show the number of points per skin depth λ_δ, global spacing d_δ in meters, number of points for local refinement r_s, local spacing d_s in meters, number of elements, and degrees of freedom (dof).

thermore, the outer boundaries are placed at least four δ away from the modeling region of interest, so that electric fields generated in the center of the computational domain are sufficiently attenuated by the artificial model boundaries, in accordance with the imposed Dirichlet boundary conditions.

Figure 2a shows a 3D variation on the model proposed by Li *et al.* (2007). We use this simple model to demonstrate the corresponding differences between adapted-meshes for $p = 1, 2, 3$. The model of interest comprises a reservoir with a finite lateral extent of 5 000 m and thickness of 100 m ($1 \cdot 10^{-2}$ S/m). The two halfspaces represent seawater (3.3 S/m) and sediments (1 S/m). Further, a simple bathymetry slope is introduced. The resulting unstructured adapted-meshes for this model are depicted in Figures 2b, 2c, and 2d. The mesh characteristics are given in Table 1, where it is easy to see the differences between each numerical scheme (e.g., the number of elements decreases for high-order polynomials which is the expected behavior). In all cases, the meshes are denser around the reservoir. They also show significant refinement in regions near the source and receivers, indicating where the mesh required refinement to improve the accuracy of the EM measurements. In this particular case, the reference model σ_p is a homogeneous background model with seawater conductivity (3.3 S/m).

2.3.2 Parallel solution of the linear system

The linear FE system that arises from eq. (5), or from eq. (16), can be written as

$$\mathbb{A}\mathbf{x} = \mathbf{b}, \tag{19}$$

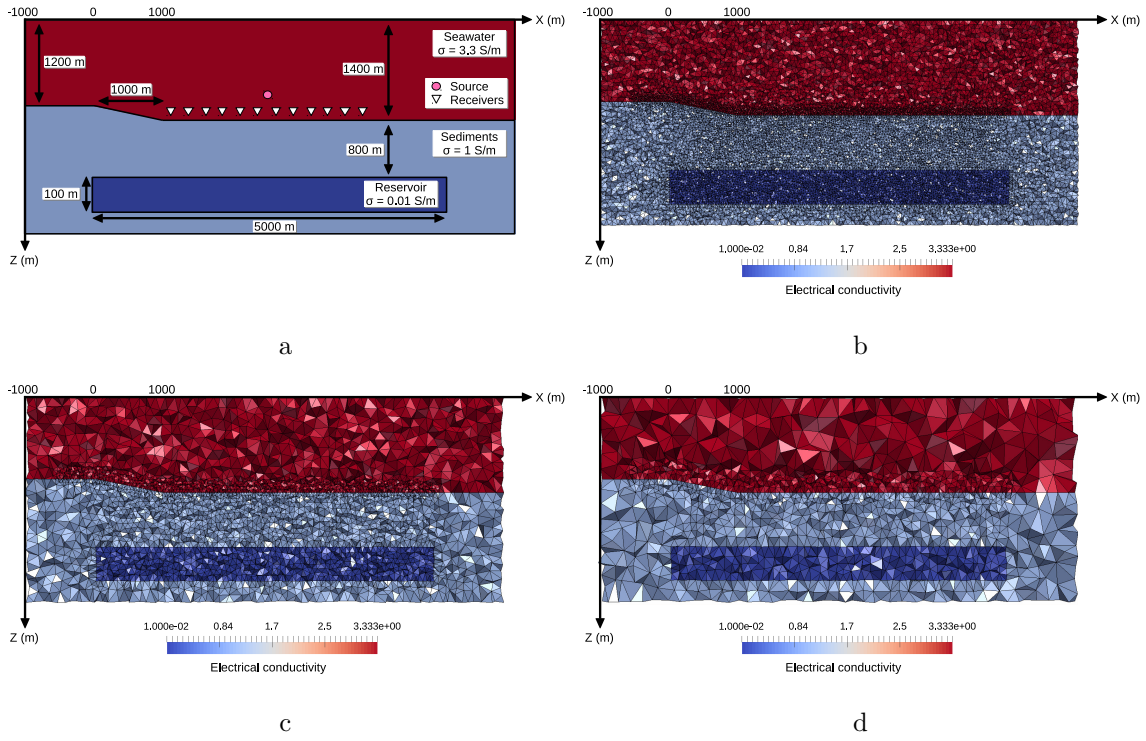

Figure 2. (a) Marine conductivity model by Li *et al.* (2007). (b) Adapted-mesh for $p = 1$. (c) Adapted-mesh for $p = 2$. (d) Adapted-mesh for $p = 3$.

where the matrix $\mathbb{A}$ represents the conductivity model discretised using the Nédélec FE method, $\mathbf{x}$ is the vector of unknowns or dof, and $\mathbf{b}$ corresponds to the source term including $\mathbf{E}_\mathrm{p}$. The matrix $\mathbb{A}$ is sparse, complex, and symmetric.

PETGEM uses the *PETSc* library (Balay *et al.* 2016) for the solution of eq. (19). This library provides a large selection of parallel iterative Krylov solvers and is well integrated in Python through the *petsc4py* package (Dalcin *et al.* 2011). Parallel constructs were implemented using the MPI standard (Fagg *et al.* 2004). MPI defines a high-level abstraction for fast and portable process communication, which is especially suited for distributed memory platforms. An MPI library is also available in Python through the *mpi4py* package (Dalcin *et al.* 2011). We refer to Castillo-Reyes *et al.* (2018) for a more detailed discussion about how *PETGEM* scales on a large parallel computer.

Marine 3D CSEM models with large conductivity contrasts (e.g., the air is several orders of magnitude more resistive than seawater or rocks) are challenging for at least two reasons. Firstly, at the low-frequency approximation considered here, solutions to the problem posed by eq. (19) can become ill-conditioned. The numerical instability is caused by the large nullspace of the curl operator as the term $i\omega\mu_0\sigma\mathbf{E}_\mathrm{s}$ becomes negligible (Schwarzbach *et al.*

2011). Secondly, large contrasts in conductivity produce jumps of the vertical electric field, causing difficulties for any discretisation method. This numerical instability is reflected in a large condition number of the linear system and often results in poor convergence for iterative Krylov solvers (Schwarzbach 2009; Key *et al.* 2011).

The Nédélec FE implementation of 2^{nd} and 3^{rd} order introduced in this paper generates a matrix $\mathbb{A}$ whose coefficients have a better conditioning number than those obtained by our preceding solutions based on Nédélec FE of 1^{st} order for the same problem (Castillo-Reyes *et al.* 2017; Castillo-Reyes *et al.* 2018).

Additionally, a preconditioning technique can further reduce the condition number of $\mathbb{A}$, thus the computation time for solving eq. (19) can be reduced. Among these preconditioners, the Jacobian and the Successive over-relaxation (SOR) preconditioners are the simplest because they do not require extra computation (Axelsson 1996). More advanced preconditioners such as Multigrid methods (Ruge and Stüben 1987; Koldan *et al.* 2014; Grayver and Kolev 2015) can be used to speed up the convergence of the iterative Krylov solvers. In this paper, we have adopted the *PETSc* implementation of the Jacobian and SOR preconditioners. These methods are simple, and they provide adequate results for the purpose of demonstrating our parallel implementation.

3 RESULTS

In order to verify our high-order Nédélec FE implementation, we simulate different scenarios of the marine 3D CSEM problem. These experiments have been performed on version IV of the *Marenostrum* supercomputer (MN4). It is a Lenovo system composed of SD530 Compute Racks, an Intel Omni-Path high performance network interconnect, and running SuSE Linux Enterprise Server as operating system. It has 165 888 processor cores at 2.10 GHz grouped into 3 456 computing nodes, 390 TB of main memory as well as 14 PB of GPFS disk storage. Each computing node has two sockets with 24 cores each for a total of 48 cores per node. Its current peak performance is 11.1 Petaflops. Furthermore, to demonstrate the versatility of the code, we use different parallel solvers.

3.1 Convergence study

As a first numerical example, a convergence study has been set up in order to validate our numerical approach and to demonstrate the potential of high-order Nédélec FE. For this experiment, we consider a two-layer model with a planar interface between seawater (3.3 S/m)

Level	Elements	d_δ	dof		
			$p=1$	$p=2$	$p=3$
1	575	355	945	4 538	12 504
2	2 182	177.5	3 289	16 276	45 507
3	12 792	88.75	17 511	89 640	254 763
4	87 998	44.37	111 995	588 880	1 694 649
5	674 308	22.18	821 863	4 392 670	12 735 345

Table 2: Mesh statistics. Number of elements, degrees of freedom (dof) and mesh spacing d_δ for each mesh level and each Nédélec FE basis polynomial degrees $p = 1, 2, 3$.

and sediments (1 S/m). The system of equations is solved using a *PETSc* implementation of the GMRES solver. Furthermore, the reference solution for a 1 Hz x-directed dipole source is computed analytically using the *DIPOLE1D* tool (Key 2009).

The numerical solutions have been computed on a set of globally refined meshes, starting from a coarse mesh with 575 elements (level 1) and ending in a fine mesh with 674 308 elements (level 5). The mesh hierarchies are given in Table 2. Polynomial-order variants on the same mesh can be considered as a global p-refinement. Therefore, three sequences of numerical solutions have been obtained using Nédélec FE basis functions with polynomial degrees $p = 1, 2, 3$. We consider an L^2-norm to quantify the errors of the numerical solution $\mathcal{Q}_h$ with respect to the analytical solution $\mathcal{Q}_e$. The L^2-norm can be stated as

$$E^s_{L^2} = \|\mathcal{Q}_h - \mathcal{Q}_e\|_{L^2(\Omega)} = \left(\int_\Omega |\mathcal{Q}_h - \mathcal{Q}_e|^2 dV \right)^{1/2}. \tag{20}$$

This norm involves the use of eq. (6) to interpolate the discrete solution to any point in the domain Ω. The convergence orders are then computed through

$$\mathcal{O}_{L^2} = \log\left(\frac{E^s_{L^2}}{E^{s-1}_{L^2}} \right) \Big/ \log\left(\frac{d^s_\delta}{d^{s-1}_\delta} \right), \tag{21}$$

where d_δ indicates the mesh spacing of the mesh level s in the sequence of meshes depicted in Table 2. The results of our convergence study are shown in Table 3. For each numerical scheme, we present the L^2 errors, the convergence orders $\mathcal{O}_{L^2}$ determined by the nested refined meshes, and the CPU times in seconds to reach the final solution on a single node of the MN4 supercomputer. For all mesh levels, the piecewise $p = 3$ approximation produces the most accurate solution, the piecewise $p = 2$ follows and the piecewise $p = 1$ the least accurate solution. Figure 3a shows the convergence results of Table 3, where it is easy to see

L^2	$\mathcal{O}_{L^2}$	CPU time (m)
	$p = 1$	
$6.5314 \cdot 10^{-2}$	—	0.05
$3.2711 \cdot 10^{-2}$	0.99	0.25
$1.6402 \cdot 10^{-2}$	0.99	1.55
$8.2410 \cdot 10^{-3}$	0.99	9.39
$4.2127 \cdot 10^{-3}$	0.98	61.43
	$p = 2$	
$3.9910 \cdot 10^{-2}$	—	0.27
$1.0211 \cdot 10^{-2}$	1.99	1.38
$2.5120 \cdot 10^{-3}$	1.99	8.81
$6.2409 \cdot 10^{-4}$	1.98	48.21
$1.5695 \cdot 10^{-4}$	1.98	286.33
	$p = 3$	
$3.6101 \cdot 10^{-2}$	—	0.54
$4.5696 \cdot 10^{-3}$	2.98	3.48
$5.7843 \cdot 10^{-4}$	2.98	23.53
$7.3219 \cdot 10^{-5}$	2.98	140.45
$9.2683 \cdot 10^{-6}$	2.98	955.35

Table 3: Convergence rates for each mesh level and each Nédélec FE basis polynomial degrees $p = 1, 2, 3$.

the convergence rates in concordance with each numerical scheme ($p = 1, 2, 3$). Furthermore, Figure 3b shows the trade-off between error and number of total dof. Although the number of dof grows faster for high-order schemes, this is compensated by the decrease in the number of elements required to achieve a certain error level (e.g., for $p = 2$ the accuracy obtained with the second mesh level is much better than $p = 1$ with third mesh level). Finally, the CPU time comparisons in Figure 3c show that high-order Nédélec FE demands more computational time for the same mesh. In view of the results in this experiment, we interpret that for moderate errors (e.g. above 2%) low-order fine-mesh approximations are better in terms of computing time. However, when higher accuracies are needed (e.g. errors below 2%), higher-order schemes are more efficient. Therefore, the optimum choice of the polynomial order depends on the input model and the required accuracy.

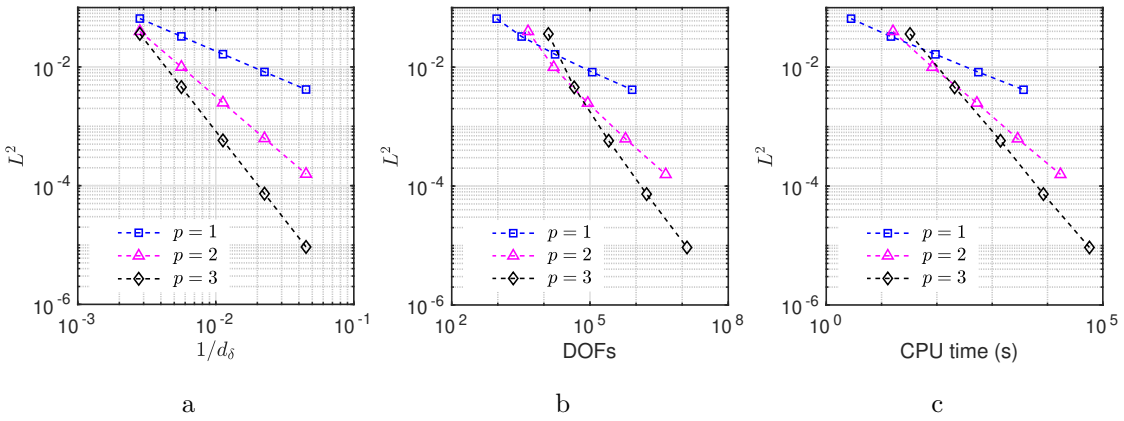

Figure 3. Convergence behavior of a sequence of refined meshes for Nédélec FE basis polynomial degrees $p = 1, 2, 3$. The L^2 is plotted versus (a) mesh spacing d_δ, (b) number of dof and (c) the CPU time.

Additionally, we compute the number of points per skin depth λ_δ and the resolution number r_s required to obtain a given error. It is an important aspect to specify the spatial resolution in the mesh (Section 2.3.1). Therefore, based on the results of our convergence study, and once three desired error levels are chosen $(2\%, 1\%, 0.5\%)$, we obtain the λ_δ and the r_s needed to achieve these accuracy thresholds for each p value. Table 4 shows λ_δ values for each Nédélec basis order p. The r_s values for each Nédélec polynomial order p are depicted in Table 5. It is worth to mention that λ_δ determines the characteristic element length in the mesh, which ensures the proper resolution of the electromagnetic wave. In Table 4 it is easy to see that λ_δ grows faster for $p = 1$ than for $p = 2, 3$ (e.g., for $p = 1$ and with respect to error levels, λ_δ grows by a factor of ≈ 2, while for $p = 2$ increases by a factor of ≈ 1.4). Furthermore, the reduction of points per skin depth is more pronounced from $p = 1$ to $p = 2$ than from $p = 2$ to $p = 3$. We point out that although λ_δ and r_s values are appropriate for generating meshes of sufficient quality for successful numerical modeling, the best performance in terms of speed and precision depends on the input model.

3.2 Canonical model with a thin resistive layer

As a second example, we use the same 1D model as Constable and Weiss (2006): A half-space composed by 1 000 m thick seawater (3.3 S/m), 1 000 m thick sediments (1 S/m), 100 m thick oil $(1 \cdot 10^{-2}$ S/m), and 1 400 m thick sediments (1 S/m). The computational domain is defined by $[-1, 4.5] \times [0, 3.5] \times [0, 3.5]$ km, resulting in an unstructured tetrahedral mesh with 33 728 elements. For the sake of clarity, Figure 4 shows a description of the 3D CSEM

Basis order	Error level		
	2%	1%	0.5%
$p = 1$	2.5382	5.0995	10.2943
$p = 2$	1.0918	1.5468	2.1877
$p = 3$	0.9433	1.1914	1.5032

Table 4: Number of points per skin depth λ_δ required to obtain a given error using Nédélec FE basis polynomial degrees $p = 1, 2, 3$.

model under consideration. For this modeling, we use a 2 Hz x-directed dipole source located at $x = 1\,750$ m, $y = 1\,750$ m, and $z = 975$ m with a moment of 1 Am. The receivers are placed in-line to the source position and along its orientation, directly above the seafloor ($z = 990$) with a spacing of 58 m. Furthermore, based on our meshing strategy, we have prepared a set of adapted meshes for each Nédélec basis $p = 1, 2, 3$. The mesh characteristics are given in Table 6 and each of them is designed to attain errors of 1% in amplitude of the electric field, following Table 4. We executed our simulations with 96 MPI tasks. Also, the systems of equations for the unknown electric field $\mathbf{E}_\mathrm{s}$ are solved using a *PETSc* implementation of the GMRES solver. To highlight the effect of the mesh quality on the modeled electromagnetic field, nine simulations have been executed for each mesh and each Nédélec FE basis order. First, Figure 5 shows the amplitude $|\mathbf{E}_x|$ and phase Φ_x of the electric field responses, along the receiver line, for each basis order p and its corresponding adapted mesh. For both quantities, the results are almost identical with respect to the reference.

Figure 6 shows a comparison of the amplitude $\epsilon(|\mathbf{E}_x|)$ and phase $\epsilon(\Phi_x)^\circ$ misfits (errors

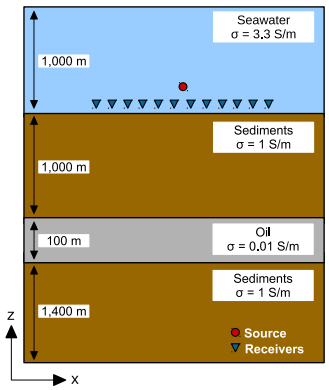

Figure 4. In-line canonical off-shore hydrocarbon 3D CSEM model by Constable and Weiss (2006).

Basis order	Error level		
	2%	1%	0.5%
$p = 1$	13	14	15
$p = 2$	11	11.8	12.5
$p = 3$	10	10.5	11.1

Table 5: Number of resolution points r_s required to obtain a given error using Nédélec FE basis polynomial degrees $p = 1, 2, 3$.

according to eq. 20) for each order p and each adapted mesh. Moreover, Table 7 shows the mean misfits for each simulation, where it is easy to see that error values are within the prescripted error level determined by the number of points per skin depth λ_δ (i.e., Table 4). For the finest mesh ($d_{\delta 1} = 69.7470$), the $p = 2, 3$ approximations produce the most accurate solutions since the characteristic mesh spacing h is smaller than expected for the numerical scheme (e.g., $d_{\delta 1} < d_{\delta 2}, d_{\delta 3}$). On the other hand, for the coarsest mesh ($d_{\delta 3} = 298.5351$) $p = 1$ provides the least accurate solution because the mesh element size is not small enough to capture the rapid change of the electric field, although in any case, the misfits do not exceed 3%. Finally, the CPU times reported in Table 7 confirm that, when high accuracies are needed, high-order schemes are more efficient regarding computing time. Therefore, we conclude that adapted meshes, in conjunction with high-order Nédélec FE basis, are highly practical and beneficial for the problem under consideration. We also give measures of phase errors, although these are not constrained by our meshing rules. Nevertheless, we consistently find phase errors smaller than amplitude errors for all simulations. Last but not least, we acknowledge unrealistically high CPU times for mesh C and $p = 3$, probably due to the solver

Label	Basis order	λ_δ	d_δ	Elements	dof
A	$p = 1$	5.0995	69.7470	949 928	1 144 996
B	$p = 2$	1.5468	229.9423	96 752	626 608
C	$p = 3$	1.1914	298.5351	57 256	1 077 120

Table 6: Mesh statistics. Points per skin depth λ_δ, mesh spacing d_δ in meters, number of elements, and degrees of freedom (dof) for each Nédélec FE basis polynomial degrees $p = 1, 2, 3$.

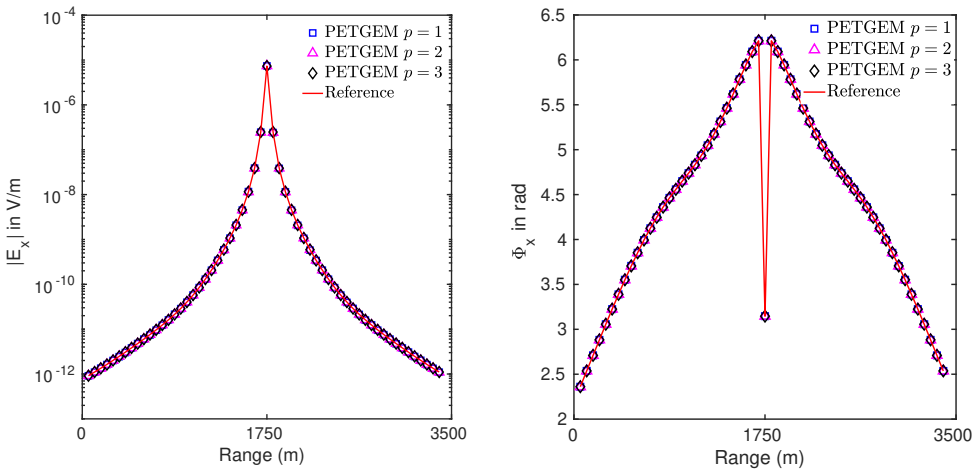

Figure 5. Comparison of in-line electric field responses obtained from *PETGEM* and *DIPOLE1D*. (a) Electric field amplitude $|\mathbf{E}_x|$. (b) Electric field phase Φ_x.

type and domain decomposition strategy. We point out that there might be combinations of other classes of iterative solvers and preconditioners that can solve the problem under consideration more efficiently. However, this is beyond the scope of this paper as we focus on the advantages of high-order Nédélec FE in conjunction with open-source libraries.

Label	Mean $\epsilon(\|\mathbf{E}_x\|)\%$			Mean $\epsilon(\Phi_x)^\circ$			CPU time (m)		
	$p=1$	$p=2$	$p=3$	$p=1$	$p=2$	$p=3$	$p=1$	$p=2$	$p=3$
A	1.11	0.50	0.39	0.19	0.10	0.10	9.09	13.55	19.47
B	2.15	1.10	0.75	0.26	0.16	0.10	4.88	5.78	9.63
C	2.86	1.38	1.08	0.29	0.21	0.16	2.05	3.83	12.17

Table 7: Mean misfits and CPU time for each order p and each adapted mesh.

3.3 3D model of an off-shore hydrocarbon reservoir

To verify the accuracy of the proposed high-order scheme, we consider the synthetic case of a 3D CSEM model with a finite target (reservoir). The model is composed by three flat-layers: 8000 m thick air ($1\cdot10^{-8}$ S/m), 2000 m thick seawater (3.3 S/m) and 10000 m thick sediments (1 S/m). The reservoir ($2\cdot10^{-2}$ S/m), with the size of $[3\,000]\times[3\,000]\times[50]$ m, is embedded in the marine sediment, centered at $x=0$ m, $y=0$ m, and $z=-2\,600$ m. The computational

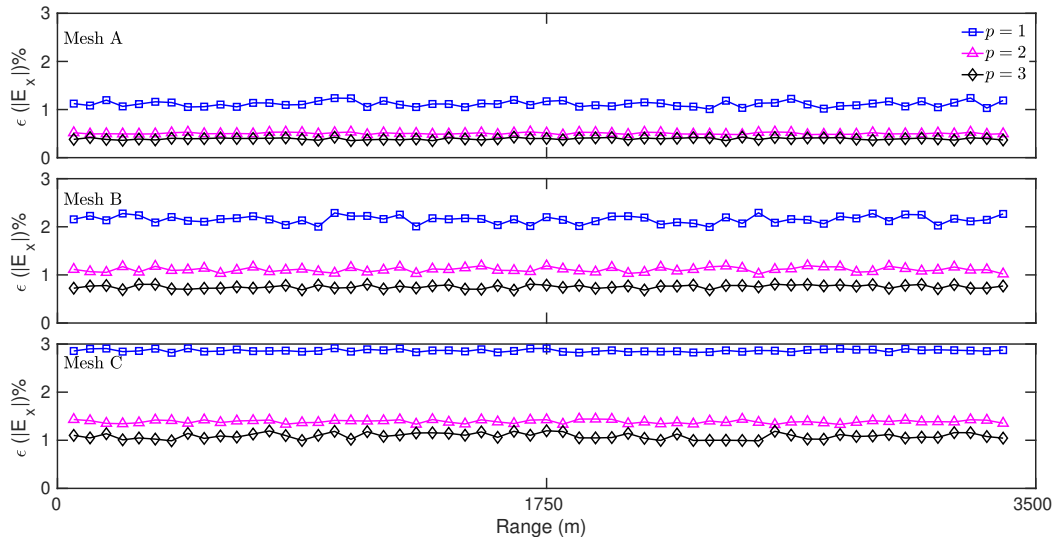

a

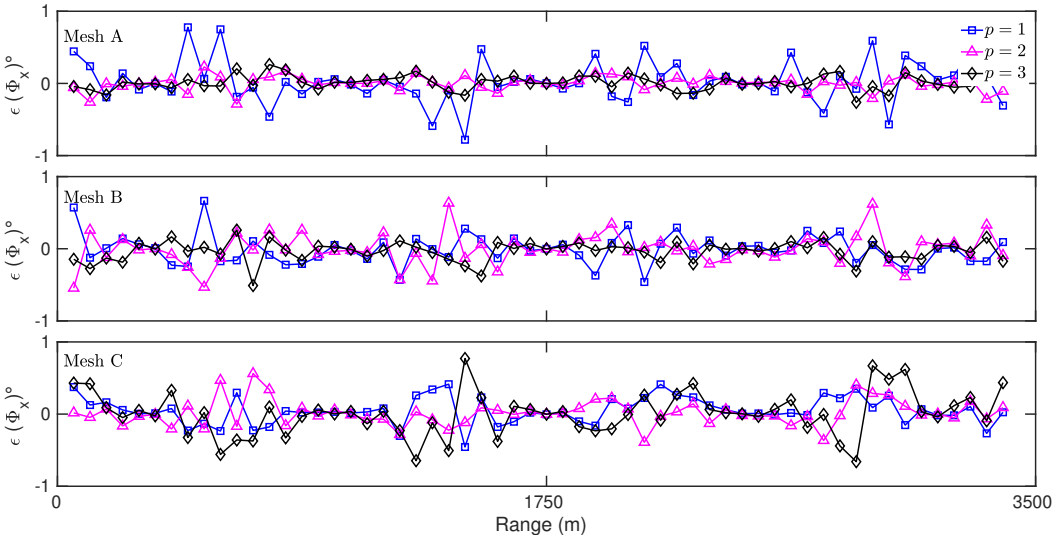

b

Figure 6. Amplitude misfit $\epsilon(|\mathbf{E}_x|)$ and phase misfit $\epsilon(\Phi_x)$ of $\mathbf{E}_x$ for $p = 1, 2, 3$ and each adapted mesh of Table 6. (a) Amplitude misfit $\epsilon(|\mathbf{E}_x|)$. (b) Phase misfit $\epsilon(\Phi_x)°$.

domain is defined by $[-15.5, 15.5] \times [-15.5, 15.5] \times [-12, 8]$ km. Figure 7 shows a 3D view of the model with its unstructured tetrahedral mesh for the halfspace $y > 18\,500$ m, where the color scale represents the electrical conductivity σ for each layer. The mesh contains 1 124 359 tetrahedral elements. In order to improve the solution accuracy, the mesh has been locally refined around regions of the sources, reservoir domain, and the seafloor, where EM data are measured by the receivers. We use four x-directed dipoles located 25 m above the seafloor at points with coordinates shown in Table 8. The frequency of the excitation current is 3 Hz

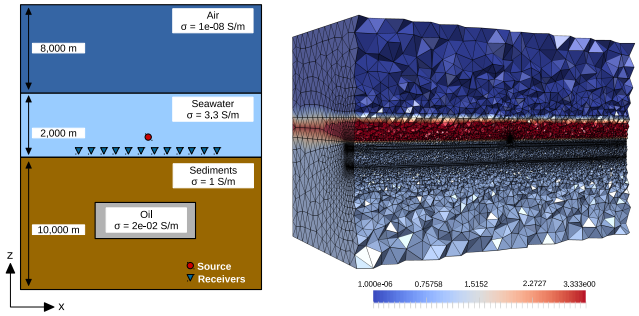

Figure 7. Synthetic marine 3D CSEM model with its unstructured tetrahedral mesh for $y > 15\,500$ m. The color scale represents the electrical conductivity σ for each layer.

with a moment of 1 Am. For this modeling case, we use 3$^{\text{rd}}$ order Nédélec FE ($p = 3$) which
374 results in 21 006 069 dof. A multifrontal parallel solver *MUMPS* (Amestoy *et al.* 2006) has been used to solve the resulting system of equations for the unknown electric field $\mathbf{E}_s$. This direct solver is supported by our modeling tool via the *PETSc* interface.

Source	x	y	z
1	$-1\,500$	0	$-1\,975$
2	-500	0	$-1\,975$
3	500	0	$-1\,975$
4	1 500	0	$-1\,975$

Table 8: Source positions for the marine 3D CSEM model shown in Figure 7. The spatial coordinates are given in meters.

376

3.3.1 In-line data analysis

378 As first analysis, we use an in-line configuration to highlight the effect of the target on the modeled electromagnetic field. The 120 receivers that are placed in-line to the source positions
380 and along their orientation, directly above the seafloor ($y = 0$ m, $z = -1\,999$ m). Figure 8 compares the amplitude $|\mathbf{E}_x|$ and phase Φ_x of the electric fields obtained from our parallel
382 modeling tool against those computed with the *BSIT* code (Hanzich *et al.* 2014), which is based on a Finite-difference (FD) approach. For both quantities, it is easy to see that the EM
384 field is distorted significantly by the target. The anomaly is observed at around $x = -1\,550$ m to $x = 1\,550$ m, which corresponds to the reservoir location.

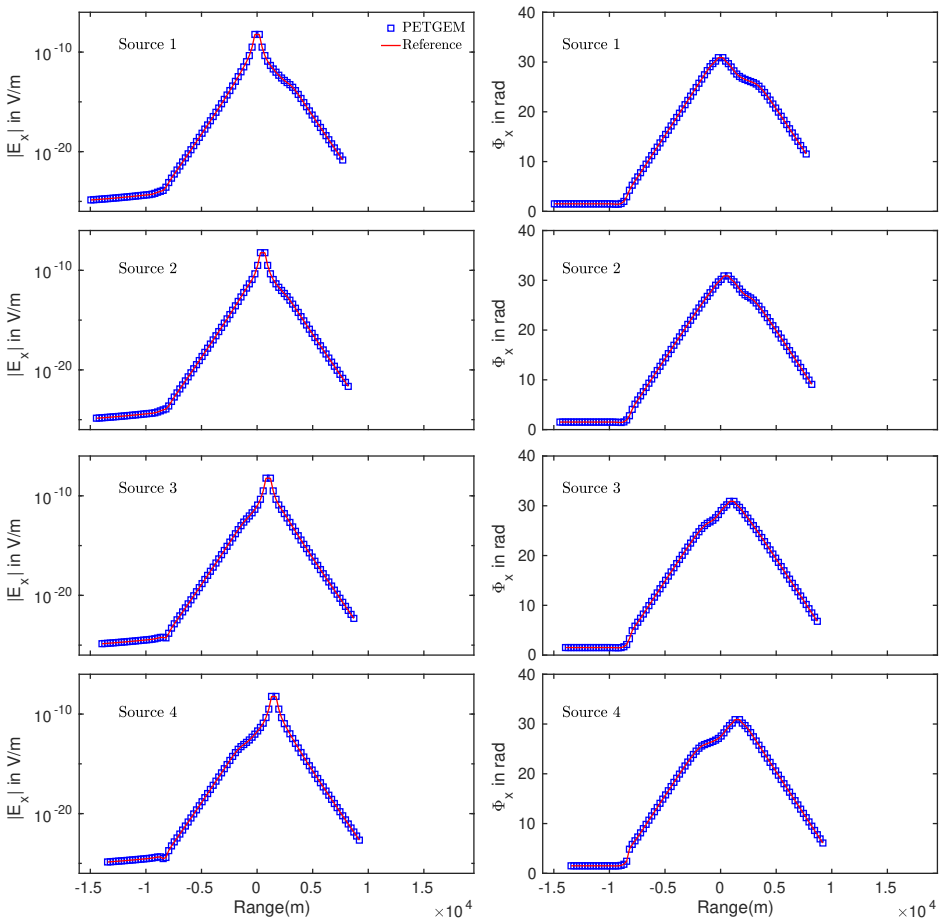

Figure 8. Amplitude $|\mathbf{E}_x|$ and phase Φ_x comparison of in-line electric field responses obtained from *PETGEM* and *BSIT*. For each source, the $|\mathbf{E}_x|$ (left panels) and Φ_x (right panels) are plotted.

As in the previous model, we compare *PETGEM* solution against the reference in terms of misfit ratios (absolute errors according to eq. 20). Figure 9 depicts the amplitude $\epsilon(|\mathbf{E}_x|)$ and phase $\epsilon(\Phi_x)^\circ$ misfits. They are all very accurate ($\approx 1\%$ of average misfits). Note that both results are subject to different numerical inaccuracy which depends on the model definition, frequencies, discretisation method, mesh quality, interpolation method, among others. As we do not have an analytical reference, we cannot verify the absolute accuracy. Nevertheless, these two completely different methods and codes agree up to maximum differences of 1%, which is an excellent result.

3.3.2 Cross-line data analysis

As a second experiment, we perform a cross-line study to show a complete analysis of the 3D EM responses. The data-acquisition region consists of 120 receivers placed cross-line to the source position and directly above the seafloor ($x = -1\,500$ m, $z = -1\,999$ m). In the following

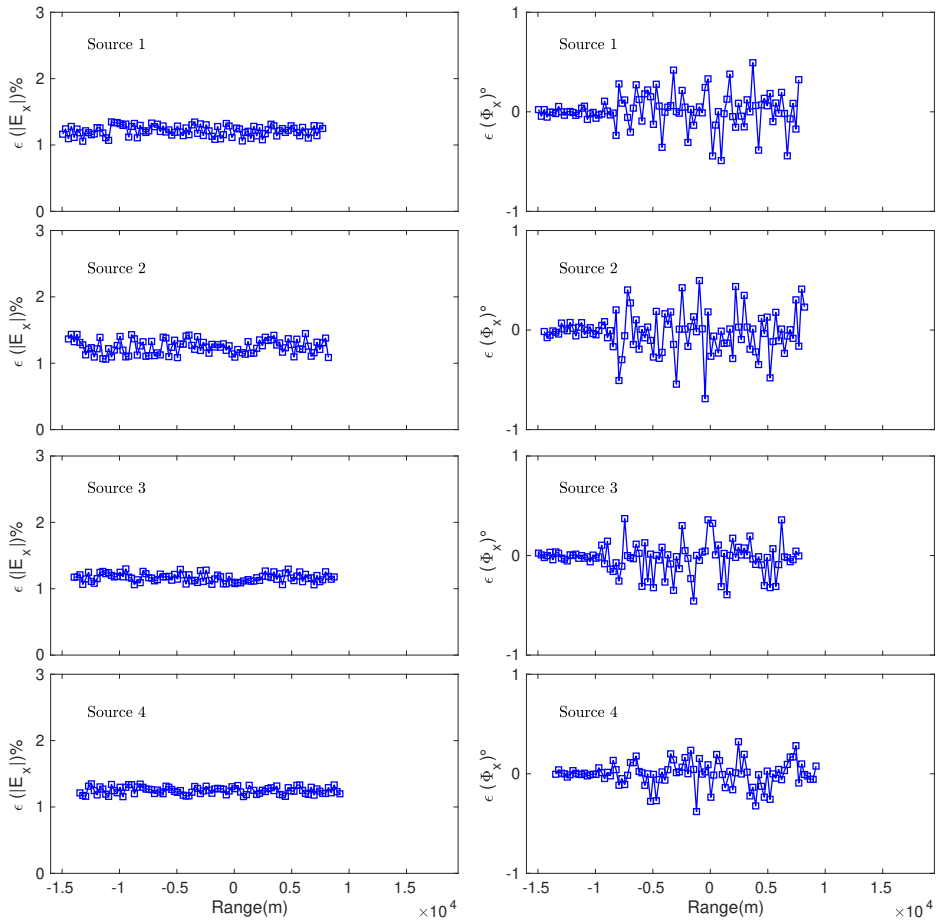

Figure 9. Amplitude misfit $\epsilon(|\mathbf{E}_x|)$ and phase misfit $\epsilon(\Phi_x)^\circ$ of $\mathbf{E}_x$ shown in Figure 8. For each source, $\epsilon(|\mathbf{E}_x|)$ (left panels) and $\epsilon(\Phi_x)^\circ$ (right panels) are plotted. In both cases, an average misfit $\approx 1\%$ is observed.

and due to the page limits, we only show the numerical modeling results for Source 2 (Table 8). The top panels of Figure 10 compares the amplitude $|\mathbf{E}_y|$ and phase Φ_y of the cross-line electric fields obtained from *BSIT* and *PETGEM*. For both quantities, the results are almost identical with respect to the reference. Furthermore, bottom panels of Figure 10 depicts the amplitude $\epsilon(|\mathbf{E}_y|)$ and phase $\epsilon(\Phi_y)^\circ$ misfits. As in previous cases, the results are very accurate ($\approx 1\%$ of average misfits). In view of the results in these experiments, we conclude that our 3D parallel modeling tool is flexible and capable to deal with realistic marine CSEM models.

3.4 Parallel performance analysis

To demonstrate the performance of the presented algorithm for large-scale 3D CSEM modeling, we consider a fine mesh for the model described in Section 3.2. In this case, we use an x-directed dipole operating at 1 Hz and a tetrahedral mesh of 4 087 808 elements. The total

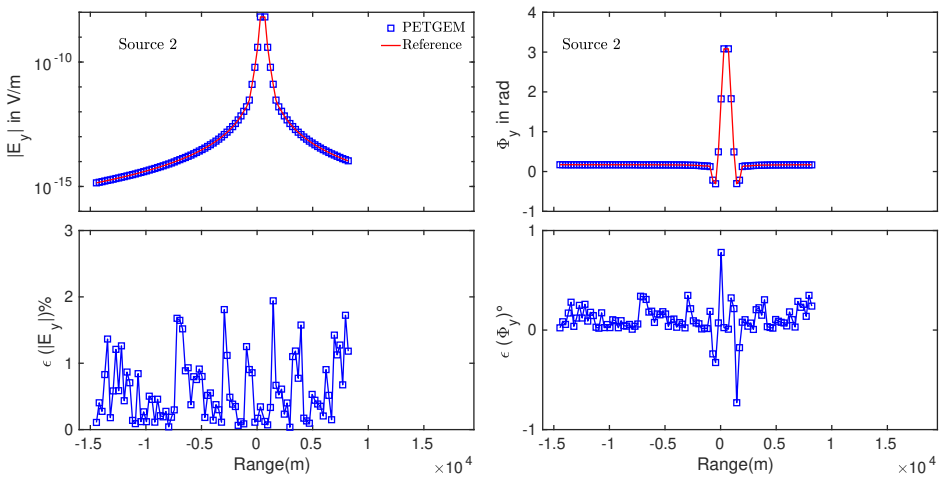

Figure 10. Cross-line electric field responses obtained from *PETGEM* and *BSIT*. The amplitude $|\mathbf{E}_y|$ and phase Φ_y fields (top panels) with its corresponding errors (bottom panels) are plotted.

number of dof is 4 872 742, 26 236 012, and 76 353 234 for $p = 1, 2, 3$, respectively. A *PETSc* implementation of the BiCGSTAB solver has been used to solve the resulting system of equations for the unknown electric field $\mathbf{E}_\mathrm{s}$. Then, the scalability of the code has been tested on distributed-memory architectures by running the same problem size for a different number of CPU, working in parallel. All simulations have been carried out on the aforementioned HPC architecture, namely the MN4 supercomputer.

The performance of our algorithm is measured based on the speed-up S, defined as the ratio of the serial CPU time T_s to the parallel CPU time T_N. The speed-up ratios are then computed through

$$S = \frac{T_\mathrm{s}}{T_\mathrm{N}}, \tag{22}$$

where N is the total number of CPUs. Furthermore, we investigate the parallel efficiency E, defined as the ratio of speed-up to N. The ratio E measures the fraction of time for which a CPU is usefully utilized and its formal definition is the following

$$E = \frac{S}{N} = \frac{T_\mathrm{s}}{N \cdot T_\mathrm{N}}. \tag{23}$$

The results of our parallel efficiency study are shown in Table 9. For each numerical scheme, we present the parallel CPU time in minutes, the speed-up S, and the parallel efficiency E. For all executions, the high-order simulations are the most efficient due to the higher workload per CPU (e.g., for $p = 1$ the resulting elemental matrices are of dimension 6×6, while for $p = 2$ of dimension 20×20, and for $p = 3$ of dimension 45×45). Figure 11a visualizes the speed-up obtained for $p = 1, 2, 3$. The achieved speed-up is almost linear for up to 1 008 CPUs. From

CPU	48	528	1008	1488	1968
		$p = 1$			
CPU time (m)	8.69	0.81	0.43	0.30	0.23
Speed-up	—	10.70	19.85	28.38	36.30
Parallel efficiency	—	0.97	0.94	0.91	0.88
		$p = 2$			
CPU time (m)	259.76	23.98	12.77	8.91	6.87
Speed-up	—	10.82	20.33	29.14	37.75
Parallel efficiency	—	0.98	0.96	0.94	0.92
		$p = 3$			
CPU time (m)	395.48	36.31	19.29	13.25	10.16
Speed-up	—	10.89	20.50	29.83	38.90
Parallel efficiency	—	0.99	0.97	0.96	0.94

Table 9: Execution results for different number of CPU and $p = 1, 2, 3$ on distributed-memory architectures.

this number on, the scalability stops its near-linear growth and slowly begins to saturate since the execution becomes dominated by exchange of messages between MPI tasks. However, the speed-up keeps growing constantly and significant reductions in runtime for more than a thousand CPUs have been observed. Furthermore, Figure 11b shows the parallel efficiency results. The comparison clearly demonstrates the performance of the parallel algorithm that we present in this paper. Although orders $p = 2, 3$ increase the CPU time required to reach the final solution, their parallel efficiency is better than for order $p = 1$. More concretely, the scalability study shows that the usage of higher-order p increases not only the accuracy for comparable computation times but also the parallel efficiency. This indicates a remarkable benefit when high-order Nédélec FE are used in conjunction with HPC approaches.

4 CONCLUSIONS

We have presented a high-order Nédélec FE approach to solve the electric field diffusion equation for arbitrary marine 3D CSEM problems under isotropic conductivities. We considered a primary/secondary electric field decomposition of the frequency-domain Maxwell's equations, where the primary field is computed for a homogeneous background model, and the secondary

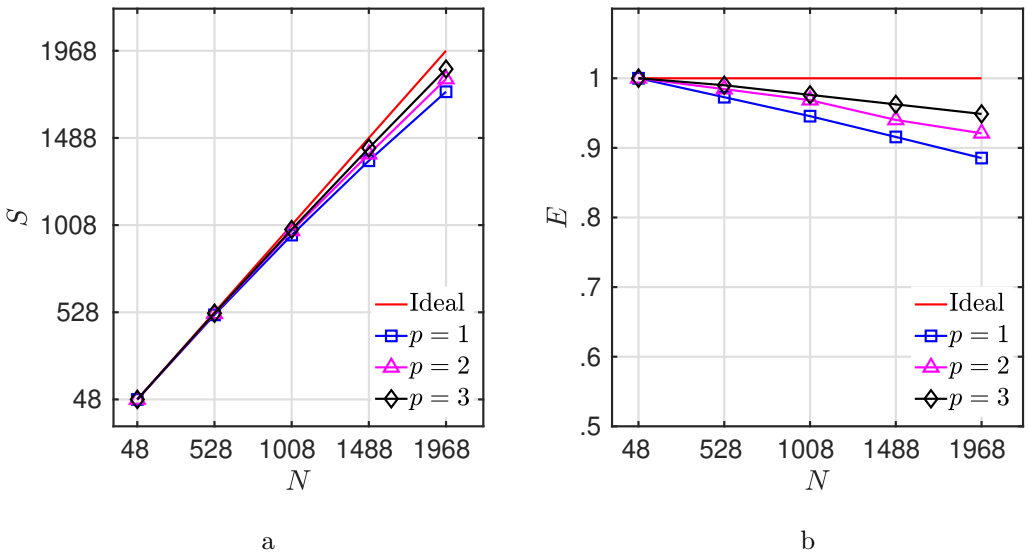

Figure 11. Visualization of the parallel efficiency results for each $p = 1, 2, 3$. The number of CPUs N is plotted versus (a) speed-up S and (b) parallel efficiency E. The computations are carried out on 48, 528, 1 008, 1 488, and 1 968 CPUs. The red line shows the theoretical ideal for comparison assuming 100% MPI efficiency.

field is consequently caused by the difference in electrical conductivity with respect to the target model. The underlying higher-order Nédélec FE have proven to be, for most applications, superior in terms of accuracy and computation times for marine 3D CSEM (and electromagnetic data in general). This high-order numerical scheme has been implemented in the kernel of *PETGEM*, and has been tested for characteristic marine CSEM model setups presented in literature. We state that this upgrated *PETGEM* is well suited to model realistic-world 3D CSEM survey data on models containing dipping layers and multiple-scale structures as well as large conductivity contrasts.

The numerical results confirm that higher-order Nédélec FE are more beneficial compared to first order polynomials. More concretely, considering decreasing error tolerances, at a certain level, the usage of the next higher-order of polynomials gives better performance in terms of computation times. Given the reasonable performance ranges for each polynomial order (e.g. Table 6), we conclude that the 2^{nd} order polynomials provides the best trade-off between mesh size and accuracy. However, the optimum choice of the polynomial order depends on the input model (e.g., target frequency, geometrical complexities, conductivity contrasts) and the required accuracy. Also, we extended our previously published adaptive-meshing technique to high-order Nédélec FE. This means, in particular, that both physical parameters and

polynomial order control mesh generation in order to satisfy the chosen quality criteria. Based on our modeling results, we conclude that adapted meshes, in conjunction with high-order Nédélec FE basis, are highly practical and beneficial for the problem under consideration. Nonetheless, we acknowledge that our conclusions should be further corroborated for more complex modeling setups.

Regarding computational efficiency, through a detailed performance scalability study, we demonstrated that our code offers an excellent parallel efficiency for actual physical phenomena. The scalability test also demonstrated that $p = 2$ has best accuracy/performance ratio for many applications, but $p = 3$ has the best parallel efficiency for massive parallelization. However, the computational efficiency depends on the solver type features (e.g., memory requirements, ability to obtain single-source or multi-source solutions, dependency on grid configuration and conductivity contrasts).

Finally, the utilization of the Python language has dramatically simplified the HPC implementation. This approach leaves more space to deal with the geophysical problem under consideration. We believe that our code's features and its open availability will prove to be useful for geophysicists interested in arbitrary marine 3D CSEM modeling and for implementing corresponding inversion routines.

5 CODE AVAILABILITY

The *PETGEM* code is freely available at the home page (*petgem.bsc.es*), at the PyPI repository (*pypi.org/project/petgem/*), at the GitHub repository (*github.com/ocastilloreyes/petgem*), or by requesting the author (*octavio.castillo@bsc.es*, *ocastilloreyes@gmail.com*). In all cases, the code is supplied in a manner to ease the immediate execution on Linux platforms. User's manual and technical documentation (developer's guide) are provided in the *PETGEM* archive as well.

6 ACKNOWLEDGEMENTS

This project has received funding from the *European Union's Horizon 2020 programme* under the *Marie Sklodowska-Curie* grant agreement No. 777778. Furthermore, the research leading to these results has received funding from the *European Union's Horizon 2020 programme* under the ChEESE Project (*https://cheese-coe.eu/*), grant agreement No. 823844. In addition, the authors would also like to thank the support of the *Ministerio de Educación y Ciencia* (Spain) under Projects TEC2016-80386-P and TIN2016-80957-P.

The authors would like to thank the Editors-in-Chief and to both reviewers, Dr. Martin Cuma and Dr. Raphael Rochlitz, for their valuable comments and suggestions which helped to improve the quality of the manuscript.

This work benefited from the valuable suggestions, comments, and proofreading of Dr. Otilio Rojas (*BSC*). Last but not least, Octavio Castillo-Reyes thanks Natalia Gutierrez (*BSC*) for her support in CSEM modeling with *BSIT*.

Author contributions: Octavio Castillo-Reyes contributed to the numerical formulation and its parallelization, Josep de la Puente designed the numerical experiments, Luis Emilio García-Castillo contributed to the math background of high-order Nédélec FE method, and José María Cela carried out the simulations and its rigorous interpretation.

APPENDIX A: HIGH-ORDER NÉDÉLEC COEFFICIENTS

Here, we include the $\boldsymbol{q}$ vectors and the coefficients for the high-order Nédélec basis (eq. (7) and (8) introduced in Section 2.2).

	Face 1	Face 2	Face 3	Face 4
$\boldsymbol{q}_1$	$(1,0,0)$	$(0,1,0)$	$(1,0,0)$	$(0,-1,1)$
$\boldsymbol{q}_2$	$(0,1,0)$	$(0,0,1)$	$(0,0,1)$	$(-1,1,0)$

Table A1: Choice of $\boldsymbol{q}$ vectors used in the coefficient computation of Nédélec basis of order $p = 2, 3$.

DOF	a_1	a_2	a_3	a_4	b_1	b_2	b_3	b_4	c_1	c_2	c_3	c_4
1	4	-6	-12	-12	0	6	0	0	0	6	0	0
2	-2	6	2	2	0	-4	0	0	0	-4	0	0
3	0	0	2	0	0	-4	0	0	0	0	0	0
4	0	0	4	0	0	-2	0	0	0	0	0	0
5	0	0	4	0	2	-2	-6	-2	0	0	4	0
6	0	0	-6	0	-4	12	6	12	0	0	-6	0
7	0	0	0	6	0	0	0	6	4	-12	-12	-6
8	0	0	0	-4	0	0	0	-4	-2	2	2	6
9	0	0	0	2	0	0	0	0	0	-4	0	0
10	0	0	0	4	0	0	0	0	0	-2	0	0
11	0	0	0	0	0	0	0	2	0	0	-4	0
12	0	0	0	0	0	0	0	4	0	0	-2	0
13	0	0	-16	0	0	8	0	0	0	0	0	0
14	0	0	-8	0	0	16	0	0	0	0	0	0
15	0	0	0	0	0	0	0	0	0	0	0	0
16	0	0	0	0	0	0	0	0	0	0	0	0
17	0	0	0	0	0	0	0	-8	0	0	16	0
18	0	0	0	0	0	0	0	16	0	0	-8	0
19	0	0	0	-16	0	0	0	0	0	8	0	0
20	0	0	0	-8	0	0	0	0	0	-8	0	0

Table A2: Coefficients corresponding to basis functions for $p = 2$ on the reference element and choice of $\boldsymbol{q}$ vectors shown in Table A1.

DOF	*D*	*E*	*F*	*G*	*H*	*I*	*J*	*K*
1	8	0	-8	-8	8	0	16	8
2	0	0	8	8	0	0	0	0
3	0	0	8	0	0	0	0	0
4	-8	0	0	0	0	0	0	0
5	-8	-8	0	0	0	0	0	0
6	8	8	-8	0	0	-8	8	-8
7	0	8	0	8	-8	-8	-8	-16
8	0	0	0	0	8	8	0	0
9	0	0	0	8	0	0	0	0
10	0	0	0	0	-8	0	0	0
11	0	8	0	0	0	0	0	0
12	0	0	0	0	0	-8	0	0
13	16	0	-8	0	0	0	16	8
14	8	0	-16	0	0	0	8	-8
15	0	0	0	0	0	0	-8	-16
16	0	0	0	0	0	0	16	8
17	0	-16	0	0	0	8	8	16
18	0	8	0	0	0	-16	8	-8
19	0	0	0	-8	16	0	16	8
20	0	0	0	8	8	0	8	-8

Table A3: Coefficients corresponding to basis functions for $p = 2$ on the reference element and choice of $\boldsymbol{q}$ vectors shown in Table A1.

DOF	a_1	a_2	a_3	a_4	a_5
1	1.47883	-4.62433	-10.48673	-10.48673	3.33333
2	0.66667	6.66667	-1	-1	-6.66667
3	0.18784	-2.04234	0.48673	0.48673	3.33333
4	0	0	-1.02117	0	0
5	0	0	-2.66667	0	0
6	0	0	-2.31216	0	0
7	0	0	0.69842	0	0
8	0	0	2.33333	0	0
9	0	0	-2.63491	0	0
10	0	0	0	2.63491	0
11	0	0	0	-2.33333	0
12	0	0	0	0.69842	0
13	0	0	0	-1.02117	0
14	0	0	0	-2.66667	0
15	0	0	0	-2.31216	0
16, . . . , 18	0	0	0	0	0
19	0	0	-60	0	0
20	0	0	-180	0	0
21	0	0	30	0	0
22	0	0	60	0	0
23	0	0	60	0	0
24	0	0	90	0	0
25 . . . 30	0	0	0	0	0
31	0	0	0	60	0
32	0	0	0	180	0
33	0	0	0	-60	0
34	0	0	0	-90	0
35	0	0	0	-30	0
36	0	0	0	-60	0
37 . . . 45	0	0	0	0	0

Table A4: Coefficients corresponding to basis functions for $p = 3$ on the reference element and choice of $\boldsymbol{q}$ vectors shown in Table A1.

DOF	a_6	a_7	a_8	a_9	a_{10}
1	0	2.63491	0	0	-7.44708
2	0	-2.33333	0	0	11.66667
3	0	0.69842	0	0	-4.21959
4	0	2.31216	0	0	-10.67456
5	0	2.66667	0	0	-8.33333
6	0	1.02117	0	0	0.99210
7	0.18784	0.48673	2.04234	0.48673	0.51579
8	0.66667	1	-6.66667	1	-6.66667
9	-1.47883	10.48673	4.62433	10.48673	-18.84913
10	0	0	0	2.63491	0
11	0	0	0	-2.33333	0
12	0	0	0	0.69842	0
13 . . . 15	0	0	0	0	0
16	0	0	0	-1.02117	0
17	0	0	0	-2.66667	0
18	0	0	0	-2.31216	0
19	0	180	0	0	-450
20	0	60	0	0	-150
21	0	-90	0	0	360
22	0	-60	0	0	240
23	0	-60	0	0	60
24	0	-30	0	0	30
25	0	0	0	-60	0
26	0	0	0	-180	0
27	0	0	0	30	0
28	0	0	0	60	0
29	0	0	0	60	0
30	0	0	0	90	0
31 . . . 45	0	0	0	0	0

Table A5: Coefficients corresponding to basis functions for $p = 3$ on the reference element and choice of $\boldsymbol{q}$ vectors shown in Table A1.

DOF	b_1	b_2	b_3	b_4	b_5
1	0	2.6349	0	0	-7.4471
2	0	-2.3333	0	0	11.6667
3	0	0.6984	0	0	-4.2196
4	0	2.3122	0	0	-10.6746
5	0	2.6667	0	0	-8.3333
6	0	1.0212	0	0	0.9921
7	0.1878	0.4867	2.0423	0.4867	0.5158
8	0.6667	1.0000	-6.6667	1.0000	-6.6667
9	-1.4788	10.4867	4.6243	10.4867	-18.8491
10	0	0	0	2.6349	0
11	0	0	0	-2.3333	0
12	0	0	0	0.6984	0
13 . . . 15	0	0	0	0	0
16	0	0	0	-1.0212	0
17	0	0	0	-2.6667	0
18	0	0	0	-2.3122	0
19	0	180	0	0	-450
20	0	60	0	0	-150
21	0	-90	0	0	360
22	0	-60	0	0	240
23	0	-60	0	0	60
24	0	-30	0	0	30
25	0	0	0	-60	0
26	0	0	0	-180	0
27	0	0	0	30	0
28	0	0	0	60	0
29	0	0	0	60	0
30	0	0	0	90	0
31 . . . 45	0	0	0	0	0

Table A6: Coefficients corresponding to basis functions for $p = 3$ on the reference element and choice of $\boldsymbol{q}$ vectors shown in Table A1.

DOF	b_6	b_7	b_8	b_9	b_{10}
1	0	0	-11.45497	-11.45497	0
2	0	0	0	0	0
3	0	0	1.45497	1.45497	0
4	0	0	-1.77251	0	0
5	0	0	-10	0	0
6	0	0	-8.22749	0	0
7	-3.33333	0.51579	1.34913	1.03158	1.34913
8	6.66667	-6.66667	16.66667	-13.33333	16.66667
9	-3.33333	-18.84913	-18.01579	-37.69825	-18.01579
10	0	-7.44708	0	-11.45497	-11.45497
11	0	11.66667	0	0	0
12	0	-4.21959	0	1.45497	1.45497
13 . . . 15	0	0	0	0	0
16	0	0.99210	0	0	8.22749
17	0	8.33333	0	0	10
18	0	10.67456	0	0	1.77251
19	0	0	-300	-450	0
20	0	0	-300	-150	0
21	0	0	60	90	0
22	0	0	120	60	0
23	0	0	360	60	0
24	0	0	240	30	0
25	0	150	0	150	300
26	0	450	0	450	300
27	0	-30	0	-30	-240
28	0	-60	0	-60	-360
29	0	-240	0	-60	-120
30	0	-360	0	-90	-60
31	0	0	0	-150	0
32	0	0	0	150	0
33	0	0	0	60	0
34	0	0	0	-30	0
35	0	0	0	30	0
36	0	0	0	-60	0
37	0	0	0	-40	0
38, 39	0	0	0	-50	0
40	0	0	0	-40	0
41, 42	0	0	0	-30	0
43	0	0	0	-180	0
44	0	0	0	540	0
45	0	0	0	-180	0

Table A7: Coefficients corresponding to basis functions for $p = 3$ on the reference element and choice of $\boldsymbol{q}$ vectors shown in Table A1.

DOF	c_1	c_2	c_3	c_4	c_5
1	0	2.63491	0	0	-7.44708
2	0	-2.33333	0	0	11.66667
3	0	0.69842	0	0	-4.21959
4 . . . 6	0	0	0	0	0
7	0	0	0.69842	0	0
8	0	0	2.33333	0	0
9	0	0	-2.63491	0	0
10	1.47883	-10.48673	-10.48673	-4.62433	18.84913
11	0.66667	-1	-1	6.66667	6.66667
12	0.18784	0.48673	0.48673	-2.04234	0.51579
13	0	2.31216	0	0	-10.67456
14	0	2.66667	0	0	-8.33333
15	0	1.02117	0	0	0.99210
16	0	0	2.31216	0	0
17	0	0	2.66667	0	0
18	0	0	1.02117	0	0
19 . . . 24	0	0	0	0	0
25	0	0	180	0	0
26	0	0	60	0	0
27	0	0	-90	0	0
28	0	0	-60	0	0
29	0	0	-60	0	0
30	0	0	-30	0	0
31	0	-180	0	0	450
32	0	-60	0	0	150
33	0	60	0	0	-60
34	0	30	0	0	-30
35	0	90	0	0	-360
36	0	60	0	0	-240
37 . . . 45	0	0	0	0	0

Table A8: Coefficients corresponding to basis functions for $p = 3$ on the reference element and choice of $\boldsymbol{q}$ vectors shown in Table A1.

DOF	c_6	c_7	c_8	c_9	c_{10}
1	0	0	-11.45497	-11.45497	0
2	0	0	0	0	0
3	0	0	1.45497	1.45497	0
4 . . . 6	0	0	0	0	0
7	4.21959	0	-1.45497	0	-1.45497
8	-11.66667	0	0	0	0
9	7.44708	0	11.45497	0	11.45497
10	18.84913	3.33333	37.69825	18.01579	18.01579
11	6.66667	-6.66667	13.33333	-16.66667	-16.66667
12	0.51579	3.33333	-1.03158	-1.34913	-1.34913
13	0	0	0	-1.77251	0
14	0	0	0	-10	0
15	0	0	0	-8.22749	0
16	-10.67456	0	0	0	-1.77251
17	-8.33333	0	0	0	-10
18	0.99210	0	0	0	-8.22749
19	0	0	150	0	0
20	0	0	-150	0	0
21	0	0	-30	0	0
22	0	0	60	0	0
23	0	0	-60	0	0
24	0	0	30	0	0
25	-450	0	-450	0	-300
26	-150	0	-150	0	-300
27	360	0	90	0	60
28	240	0	60	0	120
29	60	0	60	0	360
30	30	0	30	0	240
31	0	0	450	300	0
32	0	0	150	300	0
33	0	0	-60	-360	0
34	0	0	-30	-240	0
35	0	0	-90	-60	0
36	0	0	-60	-120	0
37	0	0	0	0	0
38	0	0	30	0	0
39	0	0	-10	0	0
40	0	0	40	0	0
41	0	0	10	0	0
42	0	0	50	0	0
43, 44	0	0	-180	0	0
45	0	0	540	0	0

Table A9: Coefficients corresponding to basis functions for $p = 3$ on the reference element and choice of $\boldsymbol{q}$ vectors shown in Table A1.

DOF	D	E	F	G	H
1	-5	9.84123	9.84123	-5	0
2	10	5	5	10	0
3	-5	0.15877	0.15877	-5	0
4	-9.84123	0.15877	0	0	0
5	-5	5	0	0	0
6	0.15877	9.84123	0	0	0
7	0.15877	5	0	0	0.15877
8	-5	-10	0	0	-5
9	-9.84123	5	0	0	-9.84123
10	0	0	-5	9.84123	-5
11	0	0	10	5	10
12	0	0	-5	0.15877	-5
13	0	0	0.15877	-9.84123	0
14	0	0	5	-5	0
15	0	0	9.84123	0.15877	0
16	0	0	0	0	0.15877
17	0	0	0	0	5
18	0	0	0	0	9.84123
19	-270	90	0	0	0
20	-90	270	0	0	0
21	270	0	0	0	0
22	180	0	0	0	0
23	0	-180	0	0	0
24	0	-270	0	0	0
25	0	0	0	0	90
26	0	0	0	0	270
27, 28	0	0	0	0	0
29	0	0	0	0	-180
30	0	0	0	0	-270
31	0	0	-90	270	0
32	0	0	-270	90	0
33	0	0	180	0	0
34	0	0	270	0	0
35	0	0	0	-270	0
36	0	0	0	-180	0
37 . . . 45	0	0	0	0	0

Table A10: Coefficients corresponding to basis functions for $p = 3$ on the reference element and choice of $\boldsymbol{q}$ vectors shown in Table A1.

DOF	II	JJ	K	L	M
1	0	-14.68246	-14.68246	0	-29.36492
2	0	10	10	0	20
3	0	4.68246	4.68246	0	9.36492
4	0	-5	0	0	0
5	0	-20	0	0	0
6	0	-5	0	0	0
7	5	4.68246	0	-4.68246	0.31754
8	-10	10	0	-10	-10
9	5	-14.68246	0	14.68246	-19.68246
10	9.84123	0	14.68246	14.68246	19.68246
11	5	0	-10	-10	10
12	0.15877	0	-4.68246	-4.68246	0.31754
13	0	0	-5	0	0
14	0	0	-20	0	0
15	0	0	-5	0	0
16	-9.84123	0	0	-5	0
17	-5	0	0	-20	0
18	0.15877	0	0	-5	0
19, 20	0	-360	0	0	-360
21	0	180	0	0	180
22	0	360	0	0	360
23	0	360	0	0	0
24	0	180	0	0	0
25	-270	0	0	-360	-180
26	-90	0	0	-360	180
27	270	0	0	180	0
28	180	0	0	360	0
29	0	0	0	360	0
30	0	0	0	180	0
31, 32	0	0	360	0	360
33	0	0	-360	0	0
34	0	0	-180	0	0
35	0	0	-180	0	-180
36	0	0	-360	0	-360
37, 38	0	0	0	0	0
39	0	0	0	0	-180
40 . . . 42	0	0	0	0	0
43	0	0	0	0	-360
44, 45	0	0	0	0	360

Table A11: Coefficients corresponding to basis functions for $p = 3$ on the reference element and choice of $\boldsymbol{q}$ vectors shown in Table A1.

DOF	N	O	P	Q	R
1	-14.68246	19.68246	-9.84123	19.68246	-9.84123
2	10	10	-5	10	-5
3	4.68246	0.31754	0.15877	0.31754	0.15877
4 . . . 6	0	0	0	0	0
7	0.15877	-9.36492	-4.68246	0.31754	0.47631
8	5	-20	-10	-10	-15
9	9.84123	29.36492	14.68246	-19.68246	-29.52369
10	29.52369	19.68246	29.52369	-29.36492	-14.68246
11	15	10	15	20	10
12	0.47631	0.31754	0.47631	9.36492	4.68246
13 . . . 18	0	0	0	0	0
19	180	360	180	-180	-270
20	-180	360	-180	180	-90
21	-90	0	0	0	0
22	180	0	0	0	0
23	0	-360	-180	0	0
24	0	-180	90	0	0
25	-270	-360	-540	360	180
26	-90	-360	-180	360	540
27	0	180	270	0	0
28	0	360	180	0	0
29	0	0	0	-360	-180
30	0	0	0	-180	-270
31	540	180	270	-360	-180
32	180	-180	90	-360	180
33	0	0	0	360	180
34	0	0	0	180	-90
35	-270	0	0	0	0
36	-180	0	0	0	0
37	0	0	0	0	-120
38	0	0	0	-180	-150
39	-30	0	0	0	0
40	120	0	0	0	0
41	0	180	30	0	0
42	0	180	150	0	0
43	-180	360	-180	360	-180
44	-180	-360	-180	360	540
45	540	360	540	-360	-180

Table A12: Coefficients corresponding to basis functions for $p = 3$ on the reference element and choice of $\boldsymbol{q}$ vectors shown in Table A1.

REFERENCES

Alumbaugh, D. L., Newman, G. A., Prevost, L., Shadid, J. N., 1996, Three-dimensional wideband electromagnetic modeling on massively parallel computers, *Radio Science*, **31**, 1–23.

Amestoy, P. R., Guermouche, A., L'Excellent, J. Y., Pralet, S., 2006. Hybrid scheduling for the parallel solution of linear systems, *Parallel Computing*, **32**, 136–156.

Adrian Amor-Martin and L. E. García-Castillo, 2016. Second-Order Nédélec Curl-Conforming Prismatic Element for Computational Electromagnetics, *IEEE Transactions on Antennas and Propagation*, **64**, 4384–4395.

Ansari, Seyedmasoud and Farquharson, Colin G., 2014. 3D finite-element forward modeling of electromagnetic data using vector and scalar potentials and unstructured grids, *Geophysics*, **79**, E149–E165.

Avdeev, Dmitry B., 2005. Three-dimensional electromagnetic modelling and inversion from theory to application, *Surveys in Geophysics*, **26**, 767–799.

Axelsson, O., 1996. *Iterative solution methods*, Cambridge University Press.

Auken, E., Christiansen, A. V., Kirkegaard, C., Fiandaca, G., Schamper, C., Behroozmand, A. A., Binley, A., Nielsen, E., Effersø, F., Christensen, N. B., Sørensen, K. I., Foged, N., and Vignoli, G., 2014. An overview of a highly versatile forward and stable inverse algorithm for airborne, ground-based and borehole electromagnetic and electric data, *Exploration Geophysics*, **46**, 223–235.

Badea, E. A., Everett, M.E., Newman, G. A., Biro, O., 2001. Finite-element analysis of controlled-source electromagnetic induction using coulomb-gauged potentials, *Geophysics*, **66**, 786–799.

Bakr, S. A., Mannseth, T., 2009. Feasibility of simplified integral equation modeling of low-frequency marine csem with a resistive target, *Geophysics*, **74**, F107–F117.

Balay, S., Abhyankar, S., Adams, M. F., Brown, J., Brune, P., Buschelman, K., Dalcin, L., Eijkhout, V., Gropp, W. D., Kaushik, D., Knepley, M. G., McInnes, L. C., Rupp, K., Smith, B. F., Zampini, S., Zhang, H., Zhang, H., 2016. Portable, Extensible Toolkit for Scientific Computation (PETSc), URL: http://www.mcs.anl.gov/petsc.

Börner, R. U., 2010. Numerical modelling in geo-electromagnetics: Advances and challenges, *Surveys in Geophysics*, **31**, 225–245.

Cai, H., Čuma, M., Zhdanov, M., 2015. Three-dimensional parallel edge-based finite element modeling of electromagnetic data with field redatuming, *SEG Technical Program Expanded Abstracts*, 1012–1017.

Cai, H., Xiong, B., Han, M., Zhdanov, M., 2014. 3D controlled-source electromagnetic modeling in anisotropic medium using edge-based finite element method, *Computers & Geosciences*, **73**, 164–176.

Castillo-Reyes, O., 2017. Edge-elements Formulation of 3D CSEM in Geophysics: A Parallel Approach, *Ph.D. thesis Polytechnic University of Catalonia*, URL: http://hdl.handle.net/10803/461190.

Castillo-Reyes, O., de la Puente, J., Cela, J. M., 2018. PETGEM: A parallel code for 3D CSEM forward

534 modeling using edge finite elements, *Computers & Geosciences*, **119**, 123–136.

Chung, Y., Son, J. S., Lee, T. J., Kim, H. J., Shin, C., 2014. Three-dimensional modelling of controlled-
536 source electromagnetic surveys using an edge finite element method with a direct solver, *Geophysical Prospecting*, **62**, 1468–1483.

538 Ciarlet, P. G., 2002. The Finite Element Methods for Elliptic Problems, *Classics in applied mathematics*, **40**, 1–511.

540 Constable, S., 2006. Marine electromagnetic methods: a new tool for offshore exploration, *The Leading Edge*, **25**, 438–444.

542 Constable, S., 2010. Ten years of marine CSEM for hydrocarbon exploration, *Geophysics*, **75**, 75A67–75A81..

544 Constable, S., Weiss, C. J., 2006. Mapping thin resistors and hydrocarbons with marine EM methods: Insights from 1D modeling, *Geophysics*, **71**, G43–G51.

546 Coppo, N., Darnet, M., Harcouet-Menou, V., Wawrzyniak, P., Manzella, A., Bretaudeau, F., Romano, G., Lagrou, D., Girard, J.F., 2016. Characterization of deep geothermal energy resources in low
548 enthalpy sedimentary basins in belgium using electro-magnetic methodscsem and MT results, *European Geothermal Congress*.

550 Dalcín, L., Paz, R., Kler, P., Cosimo, A., 2011. Parallel distributed computing using python, *Advances in Water Resources* **34**, 1124–1139.

552 Dalcín, L., Paz, R., Storti, M., Delia, J., 2008. MPI for Python: Performance improvements and MPI-2 extensions, *Parallel and Distributed Computing* **68**, 655–662.

554 Davydycheva, S., Druskin, V., Habashy, T., 2003. An efficient finite-difference scheme for electromagnetic logging in 3D anisotropic inhomogeneous media, *Geophysics*, **68**, 1525–1536.

556 Eidesmo, T., Ellingsrud, S., MacGregor, L., Constable, S., Sinha, M., Johansen, S., Kong, F., Westerdahl, H.. Sea bed logging (SBL), a new method for remote and direct identification of hydrocarbon
558 filled layers in deepwater areas, *First break*, **20**, 144–152.

Gabriel, E., Fagg, G. E., Bosilca, G., Angskun, T., Dongarra, J. J., Squyres, J. M., Sahay, V., Kam-
560 badur, P., Barrett, B., Lumsdaine, A., Castain, R. H., Daniel, D. J., Graham, R. L., Woodall, T. S., 2004. Open MPI: Goals, concept, and design of a next generation MPI implementation, *11th*
562 *European PVM/MPI Users Group Meeting*, pp. 97–104.

García-Castillo-Castillo, L. E., Ruiz-Genovés, A.J., Gómez-Revuelto, I., Salazar-Palma, M., Sarkar, T.
564 K., 2002. Third-order Nédélec curl-conforming finite element, *IEEE Transactions on Magnetics*, **38**, 2370–2372.

566 García-Castillo-Castillo, L. E., Salazar-Palma, M., 2000. Second-order Nédélec tetrahedral element for computational electromagnetics, *International Journal of Numerical Modelling: Electronic Net-*
568 *works, Devices and Fields*, **13**, 261–287.

Geuzaine, C., Remacle, J. F., 2008. Gmsh: a three-dimensional finite element mesh generator with
570 built-in pre-and post-processing facilities, URL: http://www. geuz. org/gmsh.

Girard, J. F., Coppo, N., Rohmer, J., Bourgeois, B., Naudet, V., Schmidt-Hattenberger, C., 2011. Time-lapse CSEM monitoring of the Ketzin (Germany) CO_2 injection using 2 × MAM configuration, *Energy Procedia*, **4**, 3322–3329.

Grayver, A. V., Kolev, T. V., 2015. Large-scale 3D geoelectromagnetic modeling using parallel adaptive high-order finite element method, *Geophysics*, **80**, E277–E291.

Haber, E., Heldmann, S., 2007. An octree multigrid method for quasi-static Maxwells equations with highly discontinuous coefficients, *Journal of Computational Physics*, **223**, 783–796.

Hanzich, M., Rodriguez, J., Gutierrez, N., de la Puente, J., Cela, J. M., 2014. Using HPC software frameworks for developing BSIT: a geophysical imaging tool, *Proceedings of WCCM XI, ECCM V, ECFD VI*, 2019–2030.

Hermeline, F., 2009. A finite volume method for approximating 3D diffusion operators on general meshes, *Journal of computational Physics*, **228**, 5763–5786.

Hördt, A., Dautel, S., Tezkan, B., Thern, H., 2000. Interpretation of long-offset transient electromagnetic data from the odenwald area, Germany, using two-dimensional modelling, *Geophys. J. Int.*, **140**, 577–586.

Hördt, A., Druskin, V. L., Knizhnerman, L. A., Strack, K. M., 1992. Interpretation of 3-D effects in long-offset transient electromagnetic (LOTEM) soundings in the Münsterland area/Germany, *Geophysics*, **57**, 1127–1137.

Jahandari, H., Farquharson, C. G., 2014. A finite-volume solution to the geophysical electromagnetic forward problem using unstructured grids, *Geophysics*, *79*, E287–E302.

Jahandari, H., Ansari, S., Farquharson, C. G., 2017. Comparison between staggered grid finite–volume and edge–based finite–element modelling of geophysical electromagnetic data on unstructured grids, *Journal of Applied Geophysics*, *138*, 185–197.

Jin, J., 2002. *The Finite Element Method in Electromagnetics*, Wiley.

Key, K., 2009. 1D inversion of multicomponent, multifrequency marine CSEM data: Methodology and synthetic studies for resolving thin resistive layers, *Geophysics*, **74**, F9–F20.

Key, K., Ovall, J., 2011. A parallel goal-oriented adaptive finite element method for 2.5-D electromagnetic modelling, *Geophys. J. Int.*, **186**, 137–154.

Koldan, J., Puzyrev, V., de la Puente, J., Houzeaux, G., Cela, J. M., 2014. Algebraic multigrid preconditioning within parallel finite-element solvers for 3-D electromagnetic modelling problems in geophysics, *Geophys. J. Int.*, **197**, 1442–1458.

Li, Y., Constable, S., 2007. 2D marine controlled-source electromagnetic modeling: Part 2the effect of bathymetry, *Geophysics*, **72**, WA63–WA71.

Mitsuhata, Y., 2000. 2-D electromagnetic modeling by finite-element method with a dipole source and topography, *Geophysics*, **65**, 465–475.

Nédélec, J. C., 1980. Mixed finite elements in R3, *Numerische Mathematik*, **35**, 315–341.

Newman, G. A., Alumbaugh, D. L., 1995. Frequency-domain modelling of airborne electromagnetic

608 responses using staggered finite differences, *Geophysical Prospecting*, **43**, 1021–1042.

Newman, G., Alumbaugh, D., 1997. Three-dimensional massively parallel electromagnetic inversion–I.
610 theory, *Geophys. J. Int.*, **128**, 345–354.

Newman, G. A., Commer, M., Carazzone, J. J., 2010. Imaging CSEM data in the presence of electrical
612 anisotropy, *Geophysics*, **75**, F51–F61.

Orange, A., Key, K., Constable, S., 2009. The feasibility of reservoir monitoring using time-lapse marine
614 CSEM, *Geophysics*, **74**, F21–F29.

Plessix, R. E., Darnet, M., Mulder, W., 2007. An approach for 3D multisource, multifrequency CSEM
616 modeling, *Geophysics*, **72**, SM177–SM184.

Puzyrev, V., Koldan, J., de la Puente, J., Houzeaux, G., Vázquez, M., Cela, J. M., 2013. A parallel
618 finite-element method for three-dimensional controlled-source electromagnetic forward modelling, *Geophys. J. Int.*, **193**, 678–693.

620 Reddy, J. N., 1984. *An Introduction to the Finite Element Method*, McGraw-Hill.

Rochlitz, R., Skibbe, N., Günther, T., 2018. custEM: customizable finite element simulation of complex
622 controlled-source electromagnetic data, *Geophysics*, **84(2)**, F17-F33.

Ruge, J. W., Stüben, K., 1987. Algebraic multigrid, in: Multigrid methods, *SIAM*, 73–130.

624 Salazar-Palma, M., Sarkar, T. K., Garca-Castillo, L. E., Roy, T., Djordjevic, A. R., 1998. Iterative and Self-Adaptive Finite-Elements in Electromagnetic Modeling, *Artech House Publishers*.

626 Schwarzbach, C., 2009. Stability of finite element solutions to Maxwells equations in frequency domain, *Ph.D. thesis TU Bergakademie Freiberg*, URL: http://nbn-resolving.de/urn:nbn:de:bsz:105-24780.

628 Schwarzbach, C., Börner, R. U., Spitzer, K., 2011. Three-dimensional adaptive higher order finite element simulation for geo-electromagnetics: a marine CSEM example, *Geophys. J. Int.*, **187**, 63–
630 74.

Sheard, S., Ritchie, T., Christopherson, K. R., Brand, E., 2005. Mining, environmental, petroleum,
632 and engineering industry applications of electromagnetic techniques in geophysics, *Surveys in Geophysics*, **26**, 653–669.

634 Sheriff, R. E., 2002. *Encyclopedic dictionary of applied geophysics*, Society of exploration geophysicists.

Srnka, L. J., Carazzone, J. J., Ephron, M. S., Eriksen, E. A., 2006. Remote reservoir resistivity mapping,
636 *The Leading Edge*, **25**, 972–975.

Streich, R., 2009. 3D finite-difference frequency-domain modeling of controlled-source electromagnetic
638 data: Direct solution and optimization for high accuracy, *Geophysics*, **74**, F95–F105.

Um, E. S., Harris, J.M., Alumbaugh, D. L., et al., 2010. A lorenz-gauged finite-element solution for
640 transient CSEM modeling, *SEG Annual Meeting*.

Werthmüller, D., 2017. An open-source full 3D electromagnetic modeler for 1D VTI media in Python:
642 empymod, *Geophysics*, **82**, WB9–WB19.

Xiong, Z., Tripp, A. C., 1997. 3-D electromagnetic modeling for near-surface targets using integral
644 equations, *Geophysics*, **62**, 1097–1106.

Yang, D., Oldenburg, D. W., 2012. Three-dimensional inversion of airborne time-domain electromagnetic data with applications to a porphyry deposit, *Geophysics*, **77**, B23–B34.

Zhdanov, M. S., 2009. *Geophysical electromagnetic theory and methods*. Elsevier.

Zhdanov, M. S., Lee, S. K., Yoshioka, K., 2006. Integral equation method for 3D modeling of electromagnetic fields in complex structures with inhomogeneous background conductivity, *Geophysics*, **71**, G333–G345.